Haverford College
Haverford Scholarship

Faculty Publications | Astronomy

2015

P-MaNGA: full spectral fitting and stellar population maps from prototype observations

Karen Masters
Haverford College, klmasters@haverford.edu

David T. Wilkinson

Claudia Maraston

Follow this and additional works at: https://scholarship.haverford.edu/astronomy_facpubs

Repository Citation

Masters, Karen; et al. (2015) "P-MaNGA: full spectral fitting and stellar population maps from prototype observations." Monthly Notices of the royal Astronomical Society, 449(1):328-360.

This Journal Article is brought to you for free and open access by the Astronomy at Haverford Scholarship. It has been accepted for inclusion in Faculty Publications by an authorized administrator of Haverford Scholarship. For more information, please contact nmedeiro@haverford.edu.

Monthly Notices of the ROYAL ASTRONOMICAL SOCIETY

MNRAS **449,** 328–360 (2015) doi:10.1093/mnras/stv301

P-MaNGA: full spectral fitting and stellar population maps from prototype observations

David M. Wilkinson,[1⋆] Claudia Maraston,[1] Daniel Thomas,[1] Lodovico Coccato,[1,2] Rita Tojeiro,[3] Michele Cappellari,[4] Francesco Belfiore,[5,6] Matthew Bershady,[7] Mike Blanton,[8] Kevin Bundy,[9] Sabrina Cales,[10] Brian Cherinka,[11] Niv Drory,[12] Eric Emsellem,[2,13] Hai Fu,[14] David Law,[15] Cheng Li,[16] Roberto Maiolino,[5,6] Karen Masters,[1] Christy Tremonti,[7] David Wake,[7] Enci Wang,[16] Anne-Marie Weijmans,[3] Ting Xiao,[16] Renbin Yan,[17] Kai Zhang,[16,17] Dmitry Bizyaev,[18] Jonathan Brinkmann,[18] Karen Kinemuchi,[18] Elena Malanushenko,[18] Viktor Malanushenko,[18] Daniel Oravetz,[18] Kaike Pan[18] and Audrey Simmons[18]

Affiliations are listed at the end of the paper

Accepted 2015 February 11. Received 2015 January 22; in original form 2014 October 7

ABSTRACT

MaNGA (Mapping Nearby Galaxies at Apache Point Observatory) is a 6-yr SDSS-IV (Sloan Digital Sky Survey IV) survey that will obtain resolved spectroscopy from 3600 to 10 300 Å for a representative sample of over 10 000 nearby galaxies. In this paper, we derive spatially resolved stellar population properties and radial gradients by performing full spectral fitting of observed galaxy spectra from P-MaNGA, a prototype of the MaNGA instrument. These data include spectra for 18 galaxies, covering a large range of morphological type. We derive age, metallicity, dust, and stellar mass maps, and their radial gradients, using high spectral-resolution stellar population models, and assess the impact of varying the stellar library input to the models. We introduce a method to determine dust extinction which is able to give smooth stellar mass maps even in cases of high and spatially non-uniform dust attenuation. With the spectral fitting, we produce detailed maps of stellar population properties which allow us to identify galactic features among this diverse sample such as spiral structure, smooth radial profiles with little azimuthal structure in spheroidal galaxies, and spatially distinct galaxy sub-components. In agreement with the literature, we find the gradients for galaxies identified as early type to be on average flat in age, and negative (-0.15 dex/R_e) in metallicity, whereas the gradients for late-type galaxies are on average negative in age (-0.39 dex/R_e) and flat in metallicity. We demonstrate how different levels of data quality change the precision with which radial gradients can be measured. We show how this analysis, extended to the large numbers of MaNGA galaxies, will have the potential to shed light on galaxy structure and evolution.

Key words: techniques: spectroscopic – galaxies: evolution – galaxies: formation – galaxies: general – galaxies: stellar content – galaxies: structure.

1 INTRODUCTION

Large spectroscopic surveys in the past 15 years (e.g. SDSS; York et al. 2000, GAMA; Driver et al. 2011, 2dFGRS; Folkes et al. 1999) have proved tremendously successful in deriving the physical properties of galaxies with high accuracy. Data across a range of redshift slices have been able to provide significant insight into the evolution of galaxy properties. Pairing these data with evolutionary population synthesis models (e.g. Vazdekis et al. 1996, 2010; Fioc & Rocca-Volmerange 1997; Maraston 1998; Leitherer et al. 1999; Bruzual & Charlot 2003; Thomas, Maraston & Bender

⋆ E-mail: david.wilkinson@port.ac.uk

© 2015 The Authors
Published by Oxford University Press on behalf of the Royal Astronomical Society

Downloaded from https://academic.oup.com/mnras/article-abstract/449/1/328/1317763
by Haverford College user
on 15 February 2018

2003; González Delgado et al. 2005; Conroy, Gunn & White 2009; Maraston & Strömbäck 2011; Thomas, Maraston & Johansson 2011) via a full spectral fitting method (e.g. PPXF by Cappellari & Emsellem 2004, VESPA by Tojeiro et al. 2007, PCA by Chen et al. 2012, STARLIGHT by Cid Fernandes et al. 2005, STECKMAP by Ocvirk et al. 2006), or using selected absorption lines (Thomas et al. 2005, 2010) allows the derivation of galaxy properties, such as star formation history, age of formation, metallicity, and chemical content, dust content, star formation rate, and stellar mass.

These large galaxy surveys – in order to collect large samples – could only perform single aperture observations per galaxy, typically across their central regions. Therefore, galaxy evolution properties as a function of internal structures, such as stellar population profiles across the core, disc or halo, cannot be measured, and the global properties are very sensitive to the aperture position and coverage (Iglesias-Páramo et al. 2013). Physical processes such as radial migration, higher level structure such as dust structure and clumped star formation, and signatures of merging and interactions cannot be easily constrained by single-aperture observations (Gerssen, Wilman & Christensen 2012; Wuyts et al. 2012).

In order to surpass these limitations, modern galaxy surveys use integral field spectroscopy (SAURON; Bacon et al. 2001, ATLAS^{3D}; Cappellari et al. 2011, CALIFA; Sánchez et al. 2012, SAMI; Croom et al. 2012, VENGA; Blanc et al. 2013, DiskMass; Bershady et al. 2010). This is a method by which multiple spectra of the same galaxy covering many 2D positions in the sky are obtained. This allows detailed internal information of each observed galaxy to be obtained.

Many of the previous integral field unit (IFU) surveys have been limited in the number of galaxies they have observed, meaning that detailed statistics of properties of a range of galaxy types is limited. MaNGA (Mapping Nearby Galaxies at Apache Point Observatory; Bundy et al. 2015) is designed to complement these small-sample surveys by providing spectral information for a large statistical sample of 10 000 galaxies across a range of galaxy types and morphologies, to be observed over a period of six years. MaNGA is one of the four surveys of the SDSS-IV (Sloan Digital Sky Survey IV) project. A unique feature of MaNGA with respect to other IFU surveys is its extended spectral coverage, from 3600 Å to 1μ. As is well known, the wider the spectral range the easier it is to break degeneracies such as the age/metallicity/dust degeneracies (e.g. Pforr, Maraston & Tonini 2012). Moreover, this spectral range includes absorptions features such as sodium and calcium triplet, that are important diagnostics of the initial mass function (IMF; e.g. Saglia et al. 2002; Conroy & van Dokkum 2012; Ferreras et al. 2013; Spiniello et al. 2014).

MaNGA aims to answer fundamental questions about the relative importance of stellar accretion, mergers and disc instabilities to mass assembly, the formation of bulges, the regulation of star formation, and the growth of galactic discs. In order to be able to answer these questions, the MaNGA main samples are selected to achieve a uniform spatial coverage that reaches either 1.5 R_e ('Primary+,' roughly 2/3 of the final sample) or 2.5 R_e ('Secondary,' roughly 1/3 of the final sample), see Wake et al. (in preparation) for details. The launch of the MaNGA survey was 2014 July 01, and the programme will run for six years, utilizing half of the dark time available in SDSS-IV. Details on the instrumentation including the design, testing, and assembly of the fibre-IFUs are given in Drory et al. (2015). Wake et al. (in preparation) presents the sample design, optimization, and final selection of the survey. The software and data framework as well as the reduction pipeline are described in Law et al. (in preparation). A description of the commissioning, the quality of survey observations, and further operational details will be given in Yan et al. (in preparation).

In order to test the performances of the survey in advance, preliminary 'MaNGA-type' galaxy data have been obtained with a MaNGA prototype instrument called P-MaNGA (described in detail in Section 2). The P-MaNGA data set contains 3D spectra (x position, y position, and wavelength) for 18 galaxies observed with a variety of IFU sizes and observational conditions. The P-MaNGA data were obtained through a generous donation of observing time by the SDSS-III Collaboration (Eisenstein et al. 2011). These data are described in detail in Bundy et al. (2015). P-MaNGA observations are used to understand and quantify the capabilities of MaNGA and help predicting the results we should expect from the full data set.

The physical properties of galaxies are obtained by analysing spectra with stellar population models. In this paper, we perform full spectral fitting of population models on the P-MaNGA data. We use a new full spectral fitting code, FIREFLY (Wilkinson & Maraston, in preparation) and experiment with the full suite of high-resolution stellar population models by Maraston & Strömbäck (2011), which in particular provide models for various input spectral libraries. We generate 2D stellar population maps and 1D radial profiles and analyse the results.

The paper is organized as follows. Section 2 describes the P-MaNGA observations, while Section 3 the tools of analyses used in this paper, namely the stellar population models and the fitting code. The description of our new treatment of dust reddening is also placed there, as well as the methodology to measure radial gradients. The analysis of individual stellar population maps and gradients is in Section 4. General results are in Section 5 where we include descriptions of tests we performed to assess the robustness of our work, and Section 6 presents the comparison with the other two early science P-MaNGA articles. Conclusions and discussion follow and close the paper.

2 P-MANGA OBSERVATIONS

MaNGA is both an instrument suite and a survey that uses the Sloan 2.5 m telescope (Gunn et al. 2006). By 2014 September, identical sets of MaNGA hardware were installed in six SDSS cartridges, allowing six individual plug-plates to be observed on a given night. Each MaNGA cartridge (or 'cart' for short) consists of 17 science IFUs ranging in size from 19 fibres (12.5 arcsec diameter) to 127 fibres (32.5 arcsec diameter) that patrol a 3° diameter field of view. 12 seven-fibre 'mini-bundles' are used for standard star flux calibration and 92 individual fibres for sky subtraction.

All 1423 fibres have a 2.0 arcsec core diameter and a 2.5 arcsec outer diameter and – when the cartridge is mounted to the telescope – feed the highly sensitive BOSS spectrographs (Smee et al. 2013) which provides continuous wavelength coverage from 3600 to 10 300 Å at a spectral resolution $R \sim 2000$ ($R \approx 1600$ at 4000 Å, and $R \approx 2300$ at 8500 Å) with a total system throughput of ∼25 per cent. We use subsets of this wavelength range in the spectral fitting analysis of this paper, due to the limitations of the empirical simple stellar population (SSP) models that are used, as discussed in Section 3.1, which will be expanded in future work. Details on the MaNGA hardware are given by Drory et al. (2015). Instrument commissioning began in 2014 January.

In this work, we use data obtained using the MaNGA engineering prototype instrument (P-MaNGA) in 2013 January. P-MaNGA was designed to explore a variety of instrument design options, observing strategies, and data reduction algorithms. These P-MaNGA data

Downloaded from https://academic.oup.com/mnras/article-abstract/449/1/328/1317763
by Haverford College user
on 15 February 2018

Table 1. Summary of differences between P-MaNGA (this paper) and the full MaNGA survey.

Survey	P-MaNGA	MaNGA
Target galaxy properties		
Sample size	18	$\sim 10\,000$
z	0.01 to 0.06	0.01 to 0.15
M_i/mag	-18.5 to -22.7	~ -17 to -23
R_e	0.7 to 3.4	1.5 (Primary) and 2.5 (Secondary)
Instrument design		
Flux standard type	Single 2 arcsec fibre	Mini-bundle
Fibres used per cart	560	1423
IFU distribution	$5 \times N_{19}$ (12 arcsec), $1 \times N_{61}$ (22 arcsec), $2 \times N_{127}$ (32 arcsec).	$2 \times N_{19}$ (12 arcsec), $4 \times N_{37}$ (17 arcsec), $4 \times N_{61}$ (22 arcsec), $2 \times N_{91}$ (27 arcsec), $5 \times N_{127}$ (32 arcsec), $12 \times N_7$ mini-bundles.

offer a valuable look at MaNGA's potential but differ substantially from the MaNGA survey data in several ways. We summarize these differences in Table 1 and describe them below.

First, P-MaNGA used only 560 total fibres distributed across just one of the two BOSS spectrographs. 470 of these fibres had a 2.0 arcsec diameter core, while 90 had either a 30 or 5.0 arcsec core and are not used for the present analysis. 410 of the 2-arcsec fibres were bundled into eight IFUs with three sizes: 19 fibres (N_{19}), 61 fibres (N_{61}), and 127 fibres (N_{127}). The P-MaNGA IFU complement was dramatically different from the MaNGA survey instrument, with $5 \times N_{19}$ (instead of just two), $1 \times N_{61}$ (instead of 4), $2 \times N_{127}$ (instead of five), and no 37-fibre or 91-fibre IFUs. The masses and sizes of the P-MaNGA galaxies observed are therefore not representative of the final MaNGA sample.

P-MaNGA observations were obtained for three galaxy fields using plates 6650, 6651, and 6652 (see summary in Table 2). In each case, observations were obtained in sets of three 20-min exposures dithered by roughly a fibre radius along the vertices of an equilateral triangle to provide uniform coverage across each IFU. These three fields were observed to varying depths, and in varying conditions as required by the P-MaNGA engineering tasks that they were designed for. Although plate 6650 (Field 9) was observed to a depth comparable to what will be regularly achieved during MaNGA operations, plates 6651 (Field 11) and 6652 (Field 4) are both significantly shallower than MaNGA survey data, and plate 6651 was intentionally observed at high airmass resulting in particularly poor image quality.

Some of the P-MaNGA targets were drawn from early versions of the MaNGA sample design, but in many cases P-MaNGA targets were chosen for specific reasons. In each of the three plates, one N_{127} IFU was allocated to a galaxy already observed by the

Table 2. Details of P-MaNGA galaxy sample. Galaxy nicknames are structures as p (prototype), Field number (see Table 4) – IFU bundle size, iterative name A/B/C. Properties are from the SDSS Data Release 8 data base (Aihara et al. 2011). Stellar masses are from the MPA-JHU catalogue based on Kauffmann et al. (2003a), in the Data Release 8 photometric pipeline, scaled to 3-arcsec fibre magnitudes. These are compared to our mass estimates and other mass estimates from broad-band fitting in Section 5.4. Starred galaxies (*) in groups γ and δ correspond to galaxies taken under very poor observational conditions and setup (plate 11, see Table 4), whereas other galaxies in these groups are taken with a setup that is closer to, but still poorer than, a MaNGA-like setup (plate 4, see Table 4). ◇ Morphologies of early-type (elliptical/lenticular) or late-type (spiral/irregular) are obtained through direct visual inspection of the corresponding SDSS images by the main author. † P-MaNGA galaxies in these groups meet the selection criteria for either the MaNGA primary or secondary samples as described in Bundy et al. (2015), and will be observed in MaNGA.

Nickname	MaNGAID	Bundle	RA (J2000 degrees)	Dec. (J2000 degrees)	z	log M_*	M_i (mag)	$(g-r)$ (mag)	R_e (arcsec)	R_{IFU} (R_e)	Morphological type◇
Group α: MaNGA-like conditions and setup, has been selected for MaNGA sample.†											
p9-127B	12-131835	ma008	143.7764	+21.6277	0.013	9.1	−18.5	0.51	6.8	2.4	LTG
p9-19B	12-131893	ma005	142.7900	+22.7465	0.051	10.6	−22.2	0.86	4.0	1.6	ETG
p9-19D	12-131577	ma007	142.7878	+20.9168	0.034	10.3	−21.2	0.79	3.2	2.0	ETG
p9-19E	12-131821	ma001	145.1260	+21.2538	0.024	9.7	−20.0	0.73	2.9	2.2	ETG
Group β: MaNGA-like conditions and setup, not selected by MaNGA.											
p9-127A	12-188794	ma003	143.7400	+21.7053	0.013	10.7	−21.3	0.70	23.7	0.7	LTG
p9-61A	12-188807	ma002	144.2993	+21.6692	0.019	10.1	−20.5	1.3?	9.3	1.2	ETG
Group γ: poorer conditions and/or setup than MaNGA, has been selected for MaNGA sample.†											
p4-19A	12-113557	ma004	165.0504	+36.3873	0.027	9.4	−19.5	0.49	2.5	2.5	LTG
p4-19B	12-113506	ma005	162.4946	+36.4150	0.023	9.5	−19.5	0.53	4.6	1.4	LTG
p4-19C	12-109657	ma006	164.0237	+36.9600	0.022	9.5	−19.4	0.72	4.8	1.3	ETG
p11-61A*	12-93688	ma002	208.0482	+13.9999	0.024	10.1	−20.7	0.77	7.3	1.5	LTG
p11-19B*	12-93551	ma005	207.2918	+13.3470	0.024	9.2	−19.4	0.42	2.4	2.6	LTG
Group δ: poorer conditions and/or setup than MaNGA, not selected by MaNGA.											
p4-127A	12-109661	ma003	163.9803	+36.8615	0.022	10.7	−22.1	0.84	10.3	1.6	LTG
p4-127B	12-109682	ma008	163.2461	+37.6134	0.042	11.0	−22.7	0.77	13.9	1.2	LTG
p4-61A	12-113576	ma002	164.4442	+36.2827	0.030	9.7	−20.0	0.71	3.4	3.4	LTG
p11-127A*	12-196354	ma003	207.8786	+14.0922	0.024	10.9	−22.4	0.85	17.0	1.0	LTG
p11-127B*	12-196727	ma008	209.2309	+14.1423	0.016	9.4	−19.4	0.42	9.6	1.7	LTG
p11-19A*	12-196773	ma004	207.5811	+14.1407	0.062	9.5	−21.1	0.85	1.1	2.8	LTG
p11-19C*	12-93538	ma006	206.7061	+14.4005	0.021	10.0	−20.9	0.54	2.8	2.2	LTG

Downloaded from https://academic.oup.com/mnras/article-abstract/449/1/328/1317763
by Haverford College user
on 15 February 2018

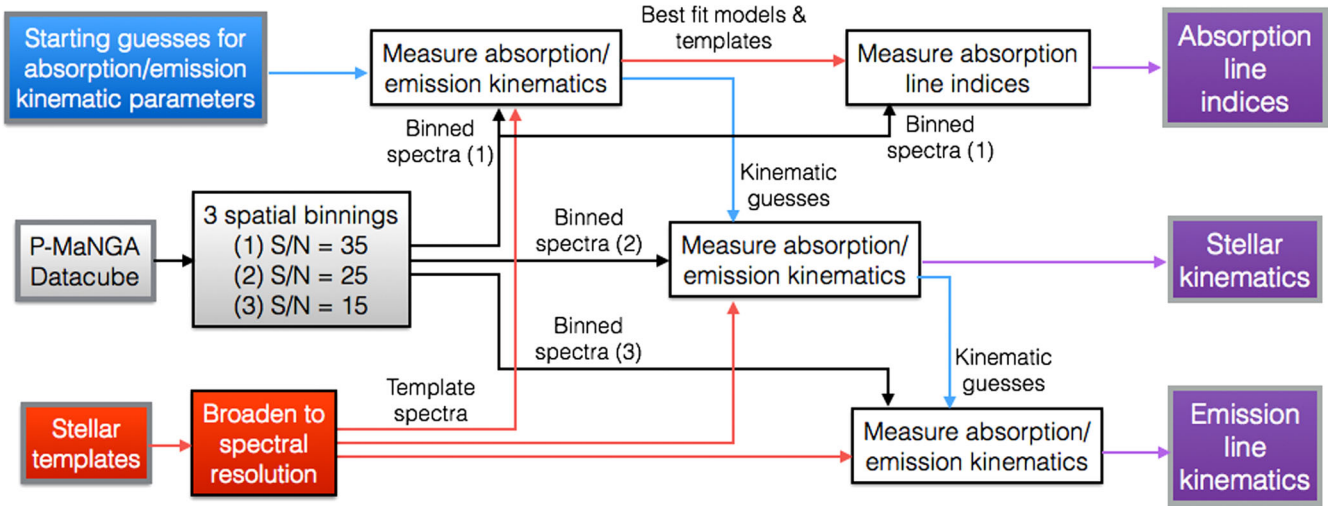

Figure 1. Summary of the processes of the PDAP, used to recover the physical parameters used as input in this work in addition to the P-MaNGA data cubes. P-MaNGA data cubes are binned in three spatial schemes according to the S/N requirements of the properties extracted from the kinematic fits. Each of the processes are described in Section 2.1. Each kinematic fit also outputs improved starting kinematic guesses for the next spatial bin.

CALIFA survey (Calar Alto Large Integral Field Area; Sánchez et al. 2012) for comparison purposes, even if it would not otherwise satisfy the MaNGA selection cuts. Additionally, the non-optimal IFU complement of the P-MaNGA instrument required some targets to be selected manually. Altogether, 18 P-MaNGA galaxies were observed (see Table 2).

The raw data were reduced using a prototype of the MaNGA data reduction pipeline (DRP), which is described in detail by Law et al. (in preparation). In brief, individual fibre flux and inverse variance spectra were extracted using a row-by-row algorithm, wavelength calibrated using a series of neon–mercury–cadmium arc lines, and flat-fielded using internal quartz calibration lamps. Sky-subtraction of the IFU fibre spectra was performed by constructing a cubic basis spline model of the sky background flux as seen by the 41 individual fibres placed on blank regions of sky, and subtracting off the resulting composite spectrum shifted to the native wavelength solution of each IFU fibre.

Flux calibration of the P-MaNGA data is performed by fitting Kurucz (1979 and revisions) model stellar spectra to the spectra of calibration standard stars covered with single fibres at each of the three dither positions. Such methods are shown from SDSS DR6 (Adelman-McCarthy et al. 2008) to yield median calibration errors over all plates of less than 2 per cent. This method is preferable to observing flux-standard stars at different times from the galaxy observations, as even on the same night systematic errors (e.g. due to changing airmass) are larger than the calibration error quoted above. The flux calibration vectors derived from these single-fibre spectra were found to vary by ∼10 per cent from exposure to exposure, depending on the amount of light lost from the fibre due to atmospheric seeing and astrometric misalignments. The flux calibration error is due to the positional error of the fibres, which can be different from plate to plate. However, error is a slowly varying function of wavelength which is absorbed by the dust method described in Section 3.3, thereby minimizing the impact on the spectral fitting. While this uncertainty is acceptable for the present science purposes, the flux calibration uncertainty of the single fibres ultimately drove the design decision of the MaNGA survey to instead use seven-fibre IFU 'mini-bundles' for each calibration standard star, which results in a photometric accuracy better than 2.5 per cent between Hα and Hβ, and better than 7 per cent between [N II] 6584 and [O II] 3726, 3729 for MaNGA survey data (see Yan et al., in preparation).

Flux calibrated spectra from the blue and red cameras were combined together across the dichroic break using an inverse-variance-weighted basis spline function. Astrometric solutions were derived for each individual fibre spectrum that incorporate information about the IFU bundle metrology (i.e. fibre location within an IFU), dithering, and atmospheric chromatic differential refraction, among other effects. Fibre spectra from all exposures for a given galaxy were then combined together into a single data cube (and corresponding inverse variance array) using these astrometric solutions and a nearest-neighbour sampling algorithm similar to that used by the CALIFA survey. For the P-MaNGA data cubes, a spaxel size of 0.5 arcsec was chosen. The typical effective spatial resolution in the reconstructed data cubes can be described by a Gaussian with FWHM ≈ 2.5 arcsec. When binning the data cubes, we scale the resulting error vectors to approximately account for wavelength and spatial covariance in the P-MaNGA error cubes. The spectral resolution is given by FWHM = 2.35σ, which is a function of wavelength as described in Smee et al. (2013). In this analysis, we use P-MaNGA data cubes, which have been processed through the prototype DRP and a prototype data analysis pipeline (PDAP) being developed at the Institute of Cosmology and Gravitation of the University of Portsmouth.[1] The relevant details are provided below.

2.1 The prototype data analysis pipeline (PDAP)

The PDAP analyses the reduced data cubes produced by the DRP to measure galaxy's physical parameters, such as kinematics and emission line fluxes. This is summarized as a flow diagram in Fig. 1 and explained in the following paragraphs.

The first analysis block within the PDAP is to spatially bin adjacent spectra to increase the signal-to-noise (S/N) ratio. This is done by using the Voronoi Binning algorithm[2] (Cappellari & Copin 2003). We implement optimal weighting to determine the S/N of

[1] For information on the PDAP contact Daniel Thomas, daniel.thomas@port.ac.uk

[2] Available from purl.org/cappellari/software

Downloaded from https://academic.oup.com/mnras/article-abstract/449/1/328/1317763
by Haverford College user
on 15 February 2018

each bin as described in Section 2.1 of Cappellari & Copin (2003), in which the weighting given to each pixel is proportional to its $S/(N^2)$. Because the various galaxy's physical parameters require different minimum S/N to be measured with a desired accuracy, the PDAP performs the spatial binning three times, producing three sets of spectra binned with different S/N criteria according to the scientific needs. These three sets of spectra are processed independently in subsequent analysis blocks, to extract the various galaxy parameters.

The S/N values quoted in the following sections are computed by calculating the median S/N per pixel over the wavelength range $5560 < \lambda/\text{Å} < 6942$, the wavelength range of the SDSS *r* band (Fukugita et al. 1996), which straddles the dichroic break of the SDSS spectrograph (Smee et al. 2013), in order to better relate to the S/N measurements in SDSS photometry. However, the binned S/N values in the P-MaNGA data do not include error covariance. Hence, the S/N thresholds in the following sections are empirically chosen to give reliable extraction of each of the corresponding properties.

The first spatial binning requires a minimum S/N = 35 per bin and is used to measure absorption line indices. This requirement is based the analysis of the errors of absorption indices as derived by Johansson, Thomas & Maraston (2012). The second spatial binning requires a minimum of S/N = 25 and is used to measure stellar kinematics. The requirement is derived from estimating the errors on kinematic parameters as in Cappellari & Emsellem (2004). The third spatial binning with a minimum S/N = 15 is used to measure the properties of the emission lines (kinematics, fluxes, equivalent widths, reddening, and Balmer decrement). This requirement is based on errors computed in Thomas et al. (2013).

The second analysis block within the PDAP fits the spatially binned spectra with a series of stellar templates and Gaussian functions. The fit is executed three times, one for each of the three groups of spatially binned spectra produced in the first analysis block.

The processes in the PDAP are applied to the full wavelength range of P-MaNGA data; however, for the spectral fitting analysis with FIREFLY, we use a large portion of this wavelength range due to the limitations of the current empirical SSP models used, as discussed in Section 3.1. In future work, we will expand this analysis to the full wavelength range.

The spectral fitting routine uses an implementation of the Penalized Pixel Fitting (hereafter, PPXF[3]; Cappellari & Emsellem 2004) and Gas AND Absorption Line Fitting (hereafter GANDALF; Sarzi et al. 2006), and it is performed into two steps. In the first step, the galaxy's ionized-gas lines are masked, and the stellar continuum is fitted with a series of SSP models from Maraston & Strömbäck (2011), which offer a large variety of calculations for various stellar libraries. In particular, the MILES-based models, which extend to ∼7000 Å are joined with the fully theoretical M11 models based on the MARCS-stellar spectra which, by having the very high spectral resolution of 0.1 Å, makes it possible to match the required high spectral resolution of MILES (2.54 Å; Beifiori et al. 2011; Falcón-Barroso et al. 2011; Prugniel, Vauglin & Koleva 2011) also in the near-IR (see Section 3.1).[3] In this first step, stellar kinematics are measured.

In the second step, the entire (unmasked) spectrum is fitted with a series of SSP models and Gaussian functions, but the stellar kinematics are kept fixed from the measurements obtained in the first step. Gaussian functions are linked into three groups, so that each group of lines have the same velocity and velocity dispersion. The three groups are (i) Balmer lines, (ii) Na I absorption lines (5890–5896 Å), (iii) all the other ionized-gas emission lines. Each gas line is broadened with a Gaussian function to match the instrumental FWHM at the wavelength that the specific line is detected at. Multiplicative and additive polynomials, or a dust attenuation law (following the prescriptions in Sarzi et al. 2006) can be added to the fit procedure in these two steps.

The first execution of the spectral fitting routine (both steps as described above) is performed on to the galaxy spectra of the first spatial binning. In this execution, sixth-order multiplicative polynomials are used to fit to the continuum. The best-fitting model of the emission lines is then removed from the galaxy binned spectra, and the strength of absorption line indices are measured. The best-fitting stellar template and the best-fitting stellar template convolved by the best-fitting stellar line-of-sight velocity dispersion are then used to correct absorption line indices for internal kinematic broadening. The best-fitting stellar and gas kinematics are used as starting guesses for the next execution of the spectral fitting routine.

The second execution (both steps as above) is performed on to the galaxy spectra of the second spatial binning. Only stellar templates that have been selected in the first execution are used. In this execution, sixth-order multiplicative polynomial and third-order additive polynomials are used for the fit. The best-fitting stellar and gas kinematics will be used as starting guesses for the next execution. The best-fitting stellar kinematics obtained in this step will be saved in the final output table, and will characterize the galaxy stellar kinematics.

The third execution of the spectral fitting routine (both steps as above) is performed to the galaxy spectra of the third spatial binning. Only stellar templates that have been selected in the first execution are used. In this execution, sixth-order multiplicative polynomial and third-order additive polynomials are used in the first step, which is a fit using PPXF. Multiplicative polynomials, or a reddening extinction law if required, are used in the second step, which is fit using an adapted version (Thomas et al. 2013) of the code GANDALF (Sarzi et al. 2006). The best-fitting gas kinematics (velocity and velocity dispersion) of each fitted emission line will be averaged together using the line flux as weight to characterize the mean gas kinematics of the galaxy. Gas-subtracted galaxy spectra are de-redshifted using the stellar kinematics measured in this third execution.

In this work, we used the PDAP to bin the galaxy spectra to reach a minimum S/N = 5, lower than the thresholds used previously since we use full spectral fitting rather than fits to emission or absorption lines. We chose S/N = 5 as it seems adequate to provide well-constrained fits, based on tests done on mock galaxy spectra in Wilkinson & Maraston (in preparation). We then fitted the binned spectra following the prescription of the third execution of the spectral fitting routine, namely to remove gas lines and to set spectra to rest frame. The gas-free, rest-framed spectra are then analysed, as described in Section 4.

3 ANALYSIS TOOLS

3.1 Models

In this work, we use the stellar population models of Maraston & Strömbäck (2011, hereafter M11) in order to match observed spectral energy distributions (SEDs) to physical properties of the stellar populations observed. We use the spectra of the base models,

[3] These extended models as the others from M11 are available at: http://www.maraston.eu/M11

Downloaded from https://academic.oup.com/mnras/article-abstract/449/1/328/1317763
by Haverford College user
on 15 February 2018

Table 3. Parameter coverage of the stellar population models as a function of input stellar library, available at http://www.maraston.eu/M11/README_M11.txt.

Model library	Wavelength coverage (min–max)/Å	Age coverage (min–max)/Myr	Metallicity coverage (Z/H)
MILES	3500–7429	6.5–15 000	[0.0001, 0.001, 0.01, 0.02, 0.04]
STELIB	3201–7900	30–15 000	[0.01, 0.02, 0.04]
ELODIE	3900–6800	3–15 000	[0.0001, 0.01, 0.02, 0.04]

i.e. SSPs. SSPs are coeval populations of stars with a given age, metallicity (in terms of [Z/H]), and IMF.

The M11 models assume the same energetics – stellar tracks and fuel consumptions in post-main sequence – as those by Maraston (2005), and in particular include the contribution of the thermally pulsating asymptotic giant branch (TP-AGB) phase (see below). The main difference is the assumed input stellar spectra, which allows the calculations of model spectra at higher spectral resolution. M11 explored all available optical empirical stellar libraries, namely MILES (Sánchez-Blázquez et al. 2006), STELIB (Le Borgne et al. 2003), and ELODIE (Prugniel et al. 2007) and also a theoretical stellar library from the MARCS (Gustafsson et al. 2008) model atmosphere calculations. The latter allows the calculation of high-resolution models also in the near-IR. The resulting stellar population parameter coverage is summarized in Table 3.[4]

A few model features are worth noticing. First, empirical libraries do not contain enough M dwarf stars to cover the full temperature and gravity extension of the theoretical main sequence from stellar tracks. M11 filled the empirical libraries with theoretical dwarf spectra from the MARCS library, smoothed to the appropriate resolution. Secondly, none of these optical empirical libraries contain carbon or oxygen-rich stars required to characterize the TP-AGB phase. M11 use the same low-resolution empirical spectra from Lançon & Wood (2000) that were used in Maraston (2005) and re-bin them via interpolation in wavelength in order to match the wavelength binning of the given library. Even if the actual resolution of those spectra remain low, the effect of the TP-AGB component on the continuum and broad features is visually identifiable in the spectra.

For the full spectral fitting analysis, we use the empirically based models because they extend down to low ages (see Table 4 and M11). This means that in practice we do not exploit the full wavelength extension of the P-MaNGA data, which we will pursue at a later stage when empirical SSP models with young stars with suitable resolution in the near-IR will be available.

An interesting finding of M11 were variations in the optical model spectra due to the input stellar library (see fig. 12 in M11). These potentially impact the galaxy properties that are obtained when different models are applied to data. For example, M11 fit the M67 globular cluster spectrum with all models finding that MILES-based models released an old (9 Gyr), half-solar metallicity best-fitting solution for this cluster, while STELIB-based models gave the parameters determined from the colour–magnitude diagram (CMD), namely 3 Gyr and solar metallicity. These findings motivate us to quantify these subtle model effects on the derived properties of the P-MaNGA data (see Section 5.5). Here, it should be noted that when we make direct comparisons between models we use the parameter coverage contained in all three of the models. This corresponds to a wavelength range of 3900–6800 Å, ages varying between 30 Myr and 15 Gyr, and metallicities of 0.5, 1.0, and 2.0 times solar metallicity. We also use two different IMFs for each of these libraries, Salpeter (Salpeter 1955) and Kroupa (Kroupa 2001). In a separate project, we plan to use the data to constrain more exotic IMFs.

[4] See http://www.maraston.eu/M11/README_M11.txt for details.

Table 4. Summary of observational conditions and setup.

Field	Groups	Conditions and setup
9	α/β	Exposure 3.0 hr, seeing 1.7 arcsec
4	γ/δ	Exposure 2.0 hr, seeing 1.3 arcsec
11	γ/δ	Exposure 1.0 hr, seeing 2.0 arcsec, (airmass ∼1.5)

3.2 Fitting method

To obtain stellar population properties from the data, we use a new full spectral fitting code, which we named FIREFLY. This was written with the purposes of mapping out inherent spectral degeneracies, working well at low S/N, comparing input stellar libraries, and making as few assumptions about the star formation histories derived as possible by modelling each star formation history as a linear combination of bursts (SSPs). The code is discussed in detail with tests to mock galaxies and example applications to SDSS galaxies in Wilkinson & Maraston (in preparation), and is summarized in this paper in the following paragraphs.

FIREFLY is a chi-squared minimization fitting code that for a given input observed SED, returns a set (typically of the order of 10^2–10^3) of model fits, each of which is a linear combination of SSPs. This set of fits is obtained through an iterative algorithm that is coded as follows.

We initially fit all base SSPs on the observed spectrum and save their chi-squared value.[5]

We then begin improving these fits, by checking if their chi-squared values are improved by adding a different SSP component with equal luminosity as the first one. For example, a 1 Gyr, solar metallicity SSP fit ($\mathrm{Fit}_1 = M_{1\ \mathrm{Gyr,Z}_\odot}$) may be improved by adding a 2 Gyr, solar metallicity component, thus creating a linear combination of SSPs as a fit to the data as $\mathrm{Fit}_2 = \frac{1}{2}\ M_{1\ \mathrm{Gyr,Z}_\odot} + \frac{1}{2}\ M_{2\ \mathrm{Gyr,\ Z}_\odot}$. Each of the possible combinations of two SSPs are checked for improvement on the one-SSP fits, and a selection of the best set of fits from both one- and two-SSP fits is saved for the next iteration. This means we are somewhat limited in the precision of weightings we can achieve with individual fits, since the smallest possible multiple of weighting on a given SSP will be given by 1/(number of iterations). However, since we construct many (of the order of 1000) possible combinations,

[5] Calculated as $\chi^2 = \sum_\lambda \frac{(O(\lambda)-M(\lambda))^2}{E(\lambda)^2}$, where O is the observed SED, M is the model SED, and E is the error spectrum, all as a function of wavelength λ.

Downloaded from https://academic.oup.com/mnras/article-abstract/449/1/328/1317763
by Haverford College user
on 15 February 2018

we can achieve a higher level of precision by combining these fits together by their probability, see below.

This process then iterates to the next step, where we check whether any of two-SSP fits can be improved with a further SSP contribution. Thus, following the convention in the example above, we may find an improved fit with $\mathrm{Fit}_3 = \frac{1}{3}\, M_{1\ \mathrm{Gyr,Z}_\odot} + \frac{1}{3}\, M_{2\ \mathrm{Gyr,\ Z}_\odot} + \frac{1}{3}\, M_{0.5\ \mathrm{Gyr,0.5\ Z}_\odot}$. Thus, we continue iteratively checking for additional SSP components until adding further SSPs no longer improves the fit. SSP components that already exist in the previous iteration of the fit can still be added to create new fits, thus allowing solutions with different weightings of SSPs.

To avoid overfitting and allow for convergence of the number of SSPs used in each linear combination, each iteration must improve on the previous fit by a statistically significant amount. To enforce this, we employ the Bayesian Information Criterion (Liddle 2007), $\mathrm{BIC} = \chi^2 + k \ln n$ at each iteration, where k is the number of fitting parameters used (in our case, the number of SSPs added in combination to make a fit), and n is the number of observations (in our case, the number of flux points used in the fit). Each iteration must reduce the BIC to be included in the output set of fits. This therefore adds a penalty term to the chi-squared value that scales linearly to the number of SSPs used in each linear combination. For the majority of FIREFLY fits of P-MaNGA data, fits converge at around the fifth iteration.

Once a set of fits is obtained, we calculate each of their stellar masses (including the subtraction of stellar mass losses and the contribution by stellar remnants as described in Maraston 1998, 2005), light-weighted and mass-weighted ages and metallicities, and the chi-squared values. We then calculate likelihoods for each of these fits by using the chi-squared cumulative probability distribution as follows:

$$P\left(X > \chi_o^2\right) = \int_{\chi_o^2}^{\mathrm{inf}} \frac{1}{2^{(k/2)}\Gamma(\frac{k}{2})} X^{(k/2)-1} \mathrm{e}^{-X/2} \mathrm{d}X, \qquad (1)$$

where Γ is the Gamma function, χ_o^2 is the critical value of chi-squared we use to find the cumulative probabilities. k is the degrees of freedom, which can be expressed as $k = N - \nu - 1$, where N is the number of (independent) observations and ν is the number of fitting parameters. Hence, for our method, N is the number of data flux points that we are fitting model fluxes to (of the order of 3000 for P-MaNGA observations), and ν is the number of SSPs used in linear combination to obtain our fits. In cases where errors are badly estimated (either over- or underestimated), resulting in a poorly constrained likelihood distribution, we assume that the error, and therefore the chi-squared values, is offset by a constant multiplicative factor in order to bring the lowest chi-squared value equal to the degrees of freedom, and re-calculate the likelihoods of the fits accordingly.

We then use these probabilities to fit a Gaussian profile[6] to each of the marginal distributions of the parameters in order to estimate their averages and standard deviations. The standard deviations are used as estimates for the errors on each of the properties. We note that the error estimate using this method will include the spectral degeneracies between the stellar population properties folded into the random errors. Generally however, higher random errors taken over a large range of different stellar populations will correspond to higher error estimates. Separating out the statistical errors on the spectra from the spectral degeneracies requires careful simulation, which will be analysed in future work. The exception to this method is the dust calculation, hence degeneracies with dust are not folded into these error estimates. The method for calculating dust is discussed in the next subsection.

We note that the errors derived in this paper are statistical plus degeneracy errors only. They do not include systematic errors from the modelling, fitting code, or covariance between pixels. For a detailed discussion of the treatment of covariance for the SAMI IFU survey, we direct the reader to Sharp et al. (2015). However, we do quantify the size of the first two of these systematic effects in Sections 5.5 and 5.6. For the effect of covariance between pixels, we note that MaNGA data will have more accurate estimation of spectral errors, allowing accurate propagation through to the final data cubes from which we can construct covariance measures between pixels, but this is beyond the time-scale of this paper. Hence, in this paper, we assume that each 2.0 arcsec fibre is an independent observation, which with dithering will increase in area slightly, to approximately 4 arcsec^2. Thus, each 0.5 arcsec spaxel of the deconstructed data cube is dependent on 15 other spaxels. Therefore, when binning data cubes in this paper, for example in elliptical bins for the radial profiles, we calculate standard areas assuming that the number of independent observations is equal to the number of grid points analysed, divided by 16. We note that always applying this 1/16 factor to the variance in each radial bin means that the overall error on a single radial bin will be an overestimate, since all 16 pixels from a given fibre may not be included in each radial bin. However, this means that the covariance between bins is therefore included in the radial profiles and thus the gradient estimations. The codependence of neighbouring pixels will be analysed in more detail in future work.

FIREFLY is able to work with either emission-cleaned spectra or implement masking over emission features as appropriate. In this paper, we use emission-cleaned spectra, as described in Section 2. GANDALF, when fitting to emission lines, also has the added benefit of releasing accurate measurements of the Doppler broadening of the SEDs due to the velocity dispersion of the stars in the object, based on PPXF fits (Cappellari & Emsellem 2004). This broadening effect essentially 'downgrades' the resolution to which we can identify absorption features in that SED, often below that of the instrumental resolution of the observation, and very often below that of the model spectra that we have used. Therefore, one needs to downgrade the model SSP resolution to match this effective resolution. In all of our analyses, this is done based on the measurement of this broadening from GANDALF with PPXF.

A particular advantage of the code when applied to P-MaNGA is the ability to map out degeneracies in age, metallicity, and dust for each individual spectrum. These effects are also explored in detail for whole-galaxy spectra in Wilkinson & Maraston (in preparation). The P-MaNGA data are binned spatially into Voronoi bins (see Cappellari & Copin 2003) in order to give a target S/N per spatial bin of 5. This gives a 2D map of 1D spectra (in other words, a 3D data cube) which are then fit individually with FIREFLY for each model combination.

3.3 Measuring dust

A feature of the code that P-MaNGA has allowed us to hone is the measurement of dust extinction. The flux calibration issues discussed in Section 2 require us to develop a more sophisticated approach to dealing with the large-scale wavelength feature of a dust attenuation curve, the measurement of which would otherwise become degenerate with the similarly large-scale feature of an

[6] Since we achieve enough fits with each run of FIREFLY, these properties are generally very well fit by Gaussian profiles.

Downloaded from https://academic.oup.com/mnras/article-abstract/449/1/328/1317763
by Haverford College user
on 15 February 2018

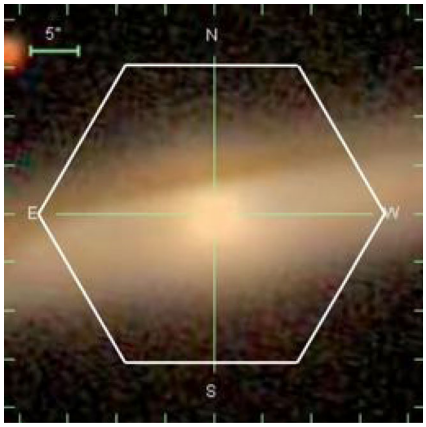

(a) SDSS imaging data with the P-MaNGA footprint in white.

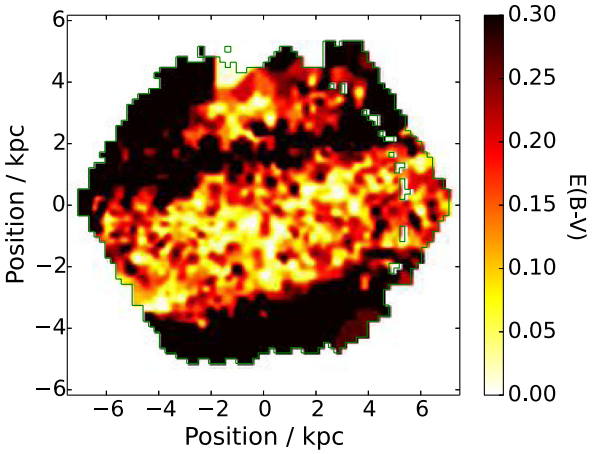

(b) Dust values obtained when folding dust in as an additional parameter to the fitting code.

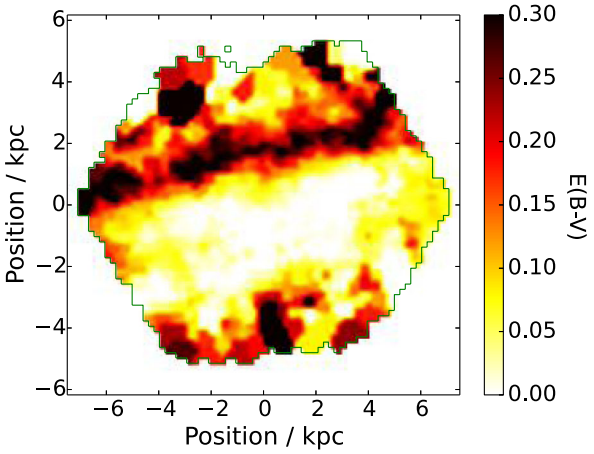

(c) Dust values obtained when using a filter to measure the dust attenuation curves before fitting the stellar population properties.

Figure 2. The effect of different methods for dealing with dust attenuation in fitting codes with the example galaxy p4-127A (in Table 2), analysed using MILES-based M11 models with its full parameter range.

unknown flux calibration curve. Visual inspection of the SDSS images corresponding to the P-MaNGA objects allows us to provide a sanity check on the results.

Consider the galaxy in Fig. 2(a), where a dust lane clearly covers the top of the P-MaNGA footprint.

One could attempt to fold in dust extinction into the fitting code by treating it as an additional free parameter to the models. However, in practice the dust–age–metallicity degeneracy together with flux calibration issues become so strong as to conspire to produce unphysical solutions. This is shown in Fig. 2(b), where the $E(B-V)$ values correspond to the value of the single parameter Calzetti law (Calzetti et al. 2000) to derive attenuation curves.[7] The $E(B-V)$ values have a high degree of scatter, are high in general, and the band of higher values that could be identified as a dust lane is clumpy and difficult to interpret. The result is clearly not an optimal representation of this galaxy.

The problem with this approach is that the large-scale shape of a spectrum is the product of both the stellar population components, the flux calibration factor, and also dust attenuation. On the other hand, the flux values of a spectrum at small scales is a result of only the stellar population components and are not sensitive to dust or flux calibration. Typically, fits to galaxy SEDs are driven by the continuum, due to it having better S/N and less noise correlation compared to individual features. Therefore, these fits are very susceptible to dust, which can become particularly problematic. If there are (even small) offsets in the continuum shape (i.e. if the continuum is flux-calibrated incorrectly or badly modelled). It can be difficult to separate out the degeneracy between dust and other stellar population properties, since both affect the overall continuum shape.

Our solution is to use an analytical function across all wavelengths to rectify the continuum before deriving the stellar population parameters. We use a functional form called high-pass filter (HPF). An HPF removes the large-scale features of a spectrum, such as continuum shape and dust extinction, through the use of a window function applied to the Fourier transform of the spectra as follows:

$$\mathrm{Flux}_\lambda^{\mathrm{output}} = \mathrm{Flux}_\lambda^{\mathrm{input}} \otimes \mathrm{W}_\lambda, \tag{2}$$

where this is the convolution in real space, and the window function $\mathrm{W}_\lambda = \mathscr{F}^{-1}\mathrm{W}_k$ describes which modes are removed by the Fourier filter, where k are the modes of the spectra. Roughly, these modes can be thought of as corresponding to features of the spectrum with wavelength size given by ∼number of wavelength points in the spectrum divided by k. Since we remove the long modes of the spectrum, we want a window function that only allows small modes. By testing the results with mock galaxies made from SSPs, we find that the following step function gives good results, with the derived properties being stable to small changes in the function:

$$\mathrm{W}_k = \begin{cases} 0 & k \le k_{\mathrm{crit}} \\ 1 & \text{otherwise}, \end{cases} \tag{3}$$

where we set $k_{\mathrm{crit}} = 40$ in this paper.

For example, a spectrum with regular wavelength intervals of 1 Å between 3000 and 9000 Å will be completely represented by 6000 modes. A filter that excludes the first 20 modes of a spectrum will therefore ignore all features in the spectrum that are larger than 6000/20 = 300 Å. The choice of modes excluded by the window function is chosen to remove potentially badly modelled or badly calibrated modes.

The step-by-step process of obtaining a dust attenuation curve is described in Fig. 3.

[7] In this paper, we shall use this form of the Calzetti law, with $R_V = 4.05$, as default in all of our derivations.

Downloaded from https://academic.oup.com/mnras/article-abstract/449/1/328/1317763
by Haverford College user
on 15 February 2018

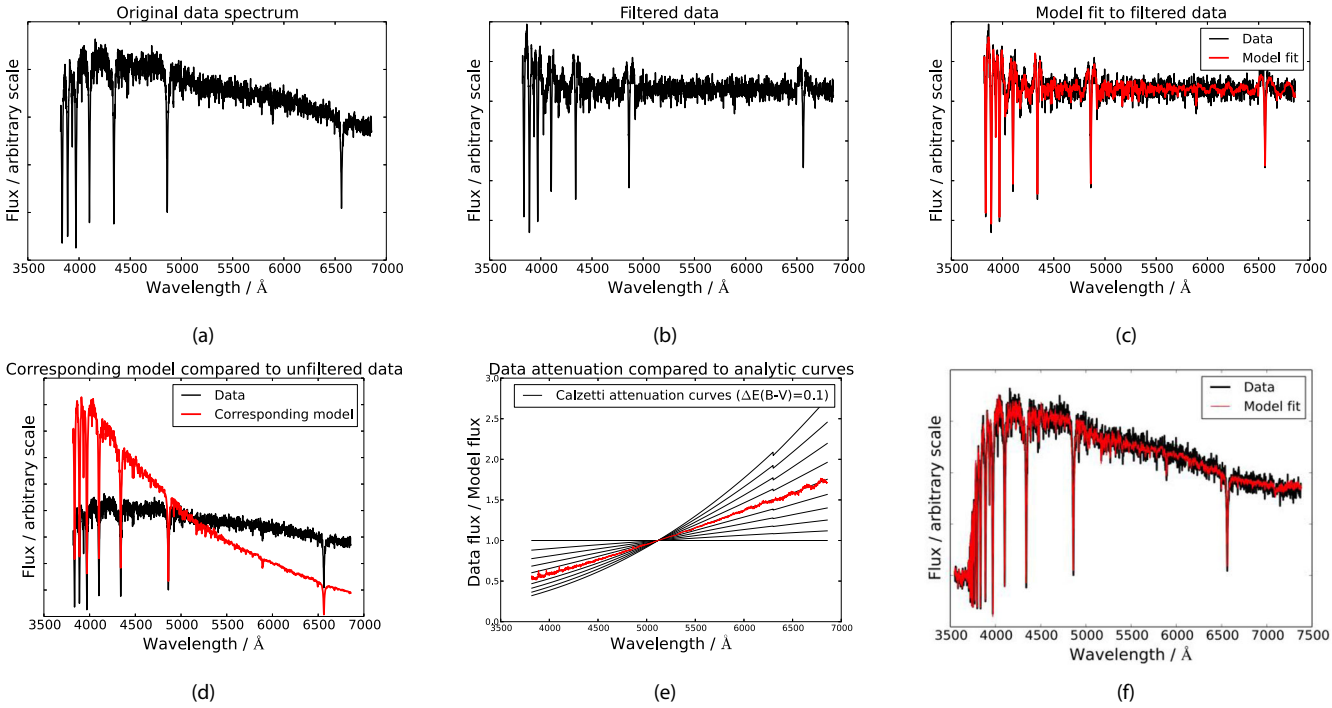

Figure 3. Example of fitting a spectrum for dust using an HPF. Starting top left and moving horizontally, the panels describe each stage of the filter and fitting process. Panel (a) shows the input model spectrum corresponding to a 30 Myr, $[Z/H] = 0$ SSP with an S/N applied at each flux point of 50. Panel (b) shows that data processed through an HPF that removes large-scale features such as continuum shape and dust extinction. Panel (c) shows the fit to the filtered spectrum using models that are filtered in the same way. All models used to make this fit have $E(B-V) = 0$ since we would be removing the effect of dust attenuation on the models anyway. Using the same parameters determined through the fit in panel (c), panel (d) shows the corresponding parameters in the unfiltered model case. We expect to see a systematic tilt between the data and models, corresponding to a dust attenuation curve. In panel (e) we find the best value for $E(B-V)$ by calculating the [data/model] spectrum and fitting this to a range of attenuation curves across the whole spectrum. In practice, we used $\Delta E(B-V)$ of 0.01, but intervals of 0.10 are shown here for clarity. The best-fitting $E(B-V)$ for this case is 0.50, exactly matching our input value of 0.50. Lastly, we use the value of $E(B-V)$ obtained to re-fit the original data using unfiltered attenuated models. Panel (f) shows the final fit obtained across the whole wavelength range.

(i) In Fig. 3(a), we show an example spectrum. This corresponds to a 30 Myr SSP from the MILES-based M11 models with a known $E(B-V)$ of 0.5, applied using the Calzetti law. We apply a Gaussian displacement on each point corresponding to S/N of 50 for clarity, although this process works as well down to S/N of 5, which is the lowest value for the P-MaNGA data outputs that we will be using in this paper. This spectrum is chosen to represent what the stellar populations of a portion of the dust lane in the galaxy in Fig. 2(a) might contain, using a known set of properties such that we can test their recovery. We apply random errors at each flux point assuming an S/N of 50.

(ii) We apply equation (2) to the data, giving the output shown in Fig. 3(b). This equation is also applied to all of the models, which are not attenuated by dust.

(iii) These filtered models are then fit to the filtered data in Fig. 3(c).

(iv) We then use the parameters measured from this fit in the unfiltered models and data (shown in Fig. 3d), dividing the best model fit by the data to give a residual attenuation curve.

(v) As shown in Fig. 3(e), we then use the dust attenuation models of Calzetti et al. (2000) to find the best matching $E(B-V)$ value that fits the recovered curve. The best-fitting model in this case returns $E(B-V) = 0.5$, exactly as input. Down to an S/N of 5, we can recover dust in mock galaxies to within 0.05 in $E(B-V)$.

(vi) The best-fitting curve is then applied to the models, which are then fit to the full unfiltered data spectrum to give the final fit in Fig. 3(f).[8]

This number of large-scale modes excluded in the fit, selected by $k_{\rm crit}$, has been tested empirically on a range of mock galaxy spectra based on SSPs. Fig. 4 shows the dust recovery, in terms of extinction in $B-V$, as a function of input age, metallicity, and extinction. Each of these properties are marginalized over the other two, meaning that, for example, the bottom plot shows the recovery of dust as a function of $k_{\rm crit}$ and dust input summed over all possible values of SSP age and metallicity input.

The plots show some dependence on dust recovered with age, visible as red or blue structure in the top plot, coming from age–dust degeneracy. However, the $E(B-V)$ values are recovered generally within a 0.03 margin within a large range of $k_{\rm crit}$ from that used in this paper. The metallicity plot shows that dust is recovered very well except when excluding modes $k_{\rm crit} > 60$, where some small dependences (<0.02 in $E(B-V)$) start to become apparent. The input dust plot, bottom, similarly shows that dust recovery is

[8] Errors on the dust extinction measured are evaluated separately to other stellar population properties since we fit this separately, and so consequently errors on age, metallicity, and stellar mass do not include errors arising from their degeneracies with dust.

Downloaded from https://academic.oup.com/mnras/article-abstract/449/1/328/1317763
by Haverford College user
on 15 February 2018

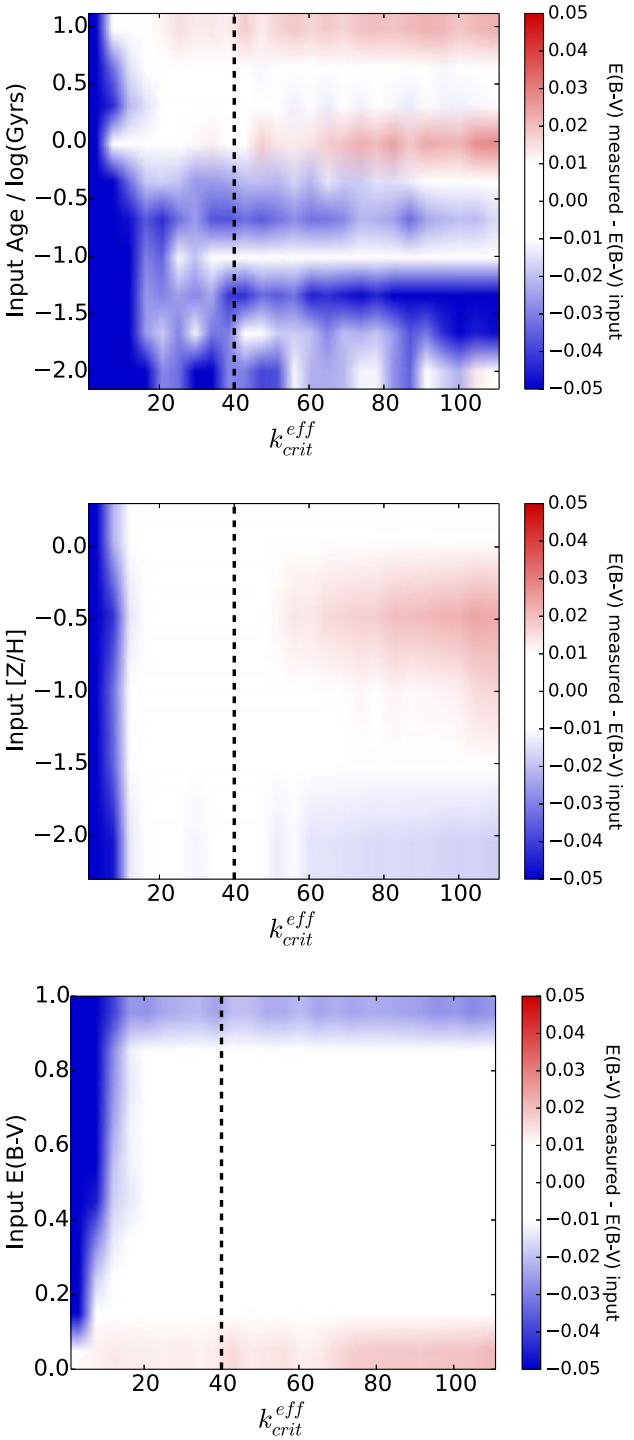

Figure 4. Tests showing the recovery of dust values [in terms of difference between $E(B-V)$ recovered to input $E(B-V)$] from mock galaxy spectra from MILES-based models as a function of the number of large-scale modes excluded in the fit. The number of modes excluded is described by an effective $k_{\rm crit}$ parameter (in equation 3). The three plots show recovery of dust as a function of the following input properties: age, metallicity, and extinction, respectively. In each case, the values plotted are marginalized over the other two input properties. The black dashed line marks the value of $k_{\rm crit}$ used in this paper for the analysis of P-MaNGA galaxies. Each mock galaxy spectra is constructed by perturbing each flux point of an input model SSP by a Gaussian probability distribution on each point, assuming a flat S/N of 10 across the whole wavelength range. An S/N of 10 was chosen as it is typical of the outer regions of most P-MaNGA galaxies.

excellent. We some edge effects where we are not able to fit below or above the dust parameter range we allow, but otherwise dust is recovered to within 0.01 in $E(B-V)$.

From these plots, we also conclude that our method gives stable solutions with small changes in the window function around the $k_{\rm crit} = 40$ value used in this paper. At around $k_{\rm crit} < 15$, we see that we almost always underestimate the amount of dust, except for low values of input dust where we cannot construct an attenuation curve to remove. Conversely, at $k_{\rm crit} > 90$, we see increasing instability in the age plot (top) as we are removing more information from our data in terms of wavelength modes used.

To properly compare with the P-MaNGA analysis, we have downgraded the wavelength sampling of the P-MaNGA spectra to match that of the wavelength sampling of the model spectra mock spectra. In these tests, we have used MILES-based models, which have been interpolated to give a constant resolution of $R = \lambda/\Delta\lambda = 4343$. The P-MaNGA spectra, with sampling of $R = 10\,000$ are therefore downgraded to the model sampling. Changing the wavelength sampling by a constant factor will change the $k_{\rm crit}$ values by that same factor accordingly. Hence, the value of the number of modes excluded is an effective $k_{\rm crit}$, written as $k^{\rm eff}_{\rm crit}$, that applies to the P-MaNGA wavelength sampling.

Mock spectra were made by taking input model SSPs and perturbing each of their flux points by an amount drawn randomly from a Gaussian probability distribution on each point given an input S/N. For these tests, we use an S/N of 10, since these represent the typical values for P-MaNGA data in the outer regions of most of the sample galaxies. We note that lowering S/N to 5 increases the errors by approximately factor 2, whereas increasing the S/N to 20 reduces the errors by approximately a factor 2, but show very similar patterns to the plots shown in Fig. 4 otherwise.

It is important to note that the particular window function used remains self-consistent as it is applied in exactly the same way to both the data and model SEDs.[9]

Using this method, we derive the dust map shown in Fig. 2(c). This is a clear improvement, as dust values are lower and more consistent, and especially show a band of higher dust values that matches the position of the observed dust lane in Fig. 2(a).

This example case shows that the functions described in equations (2) and (3) can recover dust values well despite potential flux calibration problems in at least this galaxy. We also find sensible spatially confined dust determinations for other P-MaNGA galaxies, and hence use this approach as standard in this paper. Whether this more sophisticated approach to dust attenuation is advantageous for cases where flux calibration is not thought to be a problem will be discussed in future work.

To derive radial gradients of stellar population properties, we bin the stellar population properties output by FIREFLY into elliptical annuli that are scaled in along the major axis such that the bins are constant in effective radius. From these summed properties, we derive surface mass profiles, mass-weighted stellar age profiles, and mass-weighted stellar metallicity profiles. Example profiles for the galaxy p9-19B are shown in Fig. 5.

[9] We apply the filter directly to the model SSPs, and fit combinations of these to the filtered models. This takes considerably less CPU time than applying the filter to each of the model combinations, and makes only an extremely small difference to the fluxes at each point (<0.5 per cent on any given flux point, most considerably less than this). This is because the filtering process tends towards a distributive operation at the large number of flux points on any given spectrum that we analyse.

Downloaded from https://academic.oup.com/mnras/article-abstract/449/1/328/1317763
by Haverford College user
on 15 February 2018

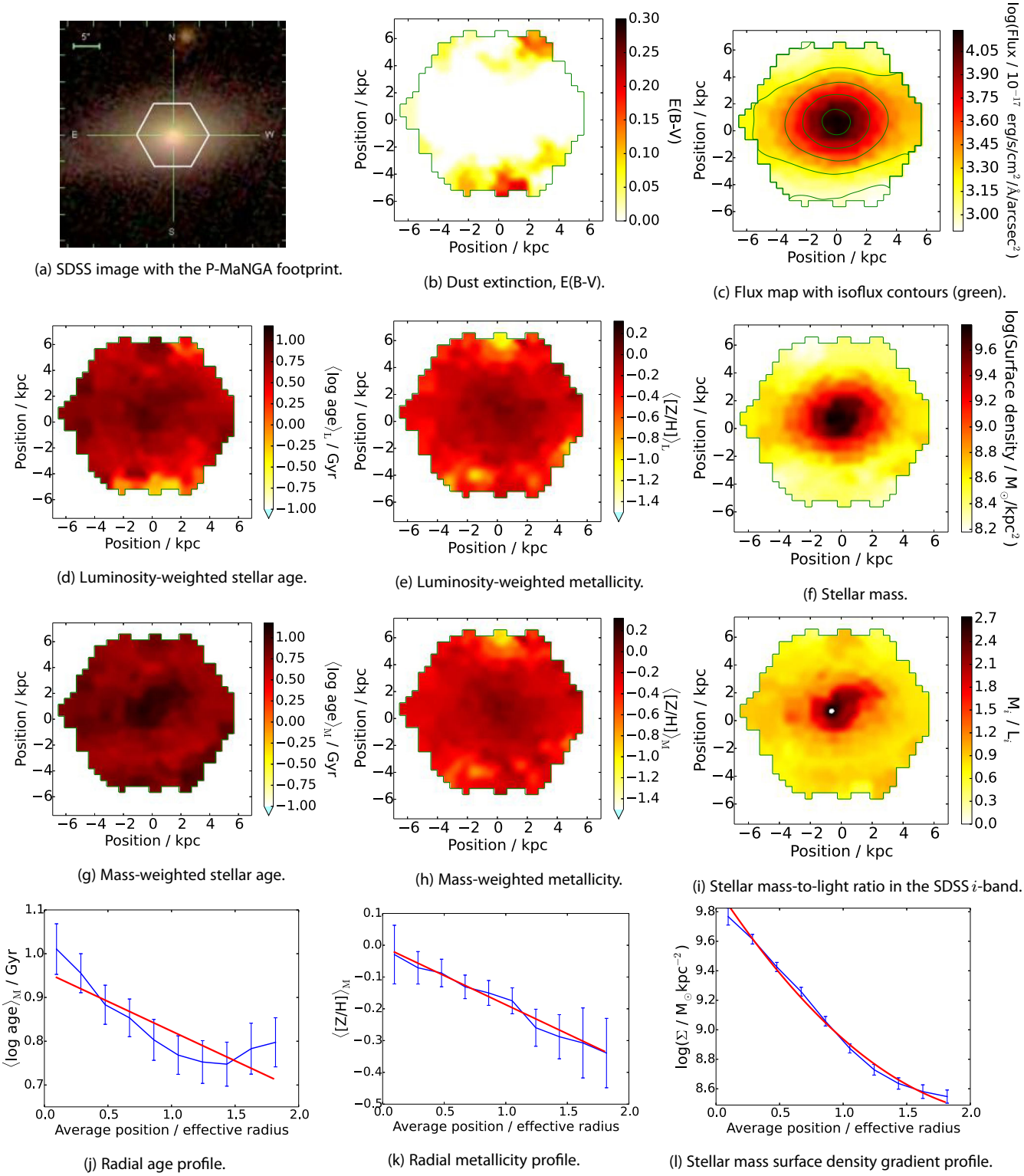

Figure 5. Group α, galaxy p9-19B as in Table 2. Stellar population maps and profiles analysed using MILES-based models with their full parameter range. The radial profiles are overplotted in red with a linear fit to the data, in the age and metallicity profiles to show the derived gradient, and a quadratic fit in the stellar mass density profile in order to guide the eye. We use a pixel-to-pixel Gaussian filter to smooth the maps for ease of visualization, but use a 0.5 σ kernel in order to retain small-scale features. This galaxy has been observed with good observational conditions with a MaNGA-like exposure time and dithering, and is selected in the MaNGA primary sample. Therefore, out of the P-MaNGA data set, these observations are the most similar to the expected output of the MaNGA primary sample.

Downloaded from https://academic.oup.com/mnras/article-abstract/449/1/328/1317763
by Haverford College user
on 15 February 2018

4 ANALYSIS OF STELLAR POPULATION MAPS

For each P-MaNGA galaxy, we derive maps of stellar mass density, light-weighted and mass-weighted stellar age and metallicity in terms of [*Z*/H], and dust extinction in terms of $E(B-V)$. We use the following conventions for denoting the age and metallicity properties: metallicities are written as $\langle[Z/H]\rangle_L$ and $\langle[Z/H]\rangle_M$ and ages are written as $\langle age\rangle_L$ and $\langle age\rangle_M$ (or $\langle \log age\rangle_L$ and $\langle \log age\rangle_M$ for the logarithmic values) for luminosity- and mass-weighted properties, respectively.

As noted above, we provide two types of stellar population maps. The first set shown in the plots are maps that are computed by weighting each stellar population component by their total luminosity across the wavelength range fitted, and find the geometric average of this to compute 'light-weighted' properties as a function of position. The second set of maps and also the radial profiles are computed by weighting each stellar population component by their stellar mass contribution, again finding the geometric average of this to compute 'mass-weighted' properties.

In this paper, we show both mass- and light-weighted properties since they can complement each other well to identify certain processes more clearly. For example, recent star formation will dramatically reduce the light-weighted stellar age deduced due to the high luminosity it contributes, despite perhaps being a very small mass component. A featureless $\langle age\rangle_M$ map with a steep negative $\langle age\rangle_L$ gradient can thus be interpreted as a galaxy that has most of its stars distributed uniformly across the galaxy but with some more star formation in its outer regions. We discuss case-by-case where these differences are greatest. Conversely, small or negligible differences in light- and mass-weighted properties come from having star formation histories that are well represented by a single-burst of star formation at its formation. Moderate differences can therefore be interpreted as having extended episode(s) of star formation. We note that FIREFLY fits stellar population components using their light contributed, and thus mass-weighted properties are decoded from the light-weighted properties by calculating the mass-to-light ratio of each stellar population component.

In all radial profile plots and analysis of gradients, we use mass-weighted property values since these give insight into the mass assembly history of the galaxies. Mass-weighted properties better trace the whole evolutionary history of the galaxy, rather than being highly affected by phases contributing a high proportion of light, such as recent star formation.

In the following sections, we will discuss some of the features identified in the stellar population maps by grouping galaxies by their similarity in data quality to the full MaNGA samples, both primary and secondary, and whether they would be included in the MaNGA target selection. Since in this work we do not calculate covariance between pixels due to the preliminary nature of the error estimates on the spectra, as discussed in Section 3.2, we calculate the statistical standard errors on the gradients obtained assuming that each pixel is dependent on 15 other pixels that in total represent a dithered 2.0 arcsec fibre observation.

After discussing each of the groups (α to δ) from Table 2 separately in this section, we provide summary plots in Section 5 showing the gradients obtained across the whole sample and the statistical errors obtained on the profiles derived as a function of observational condition. We then test the stability of the results obtained as a function of stellar library. Lastly, we compare with literature values for both total stellar mass and detailed IFU stellar population information.

4.1 MaNGA-selected galaxies with high-quality data: Group α

Two galaxies from P-MaNGA – p9-19B (Fig. 5) and p9-19D (Fig. A1) – fall into the MaNGA primary sample selection whilst also maintaining MaNGA-like data quality with 3 h exposures and decent (1.7 arcsec) seeing conditions. Both have been observed with the N_{19} IFU setup.

These galaxies are visually identified as early-type galaxies and indeed show a high level of radial symmetry in their age, metallicity, and stellar mass density maps.

Galaxy p9-19B has a $\langle \log age\rangle_L = 8$ Gyr/$\langle \log age\rangle_M = 10$ Gyr, slightly supersolar metallicity core going down to $\langle \log age\rangle_L = \langle \log age\rangle_M = 5$ Gyr with sub-solar metallicity at above 1 effective radius, and is largely dustless except for at very high radii along the minor axis. Galaxy p9-19D is similar but with a weaker age and metallicity gradient.

In both of these cases, we recover extremely smooth negative stellar population profiles with very low errors on each point, with the median of errors of 0.05, 0.10 dex in age, 0.05, 0.08 dex in metallicity, and 0.03, 0.07 dex in surface mass density for p9-19B and p9-19D, respectively. This results in errors on their respective gradients determined to 0.03, 0.05 dex/$R_e$in age and 0.05–0.09 dex/$R_e$in metallicity, which bodes well for MaNGA observations of early-type galaxies like these.

Two further galaxies from P-MaNGA fall into the MaNGA secondary sample, having wider radial coverage. The stellar population maps and profiles of these galaxies are shown and described in the appendix.We note for both of these cases the more complex nature of the stellar populations as a function of position, coupled with the lower spatial resolution than the MaNGA primary sample, means that the uncertainties on the profiles derived are greater. Profiles are determined to a median of 0.14, 0.11 dex in age, 0.24, 0.17 dex in metallicity, and 0.10, 0.07 dex in stellar mass density, corresponding to errors on the gradients to be 0.07, 0.07 dex/$R_e$in age and 0.14, 0.13 dex/$R_e$in metallicity, for p9-19E and p9-127B, respectively. This still allows recovery of significant gradients in all cases, showing that the MaNGA secondary sample should be able to find a good sample of clearly defined age gradients though may find difficulties for weak metallicity gradients.

4.2 Non-MaNGA galaxies with high-quality data: Group β

The last two galaxies from the high-quality sub-sample of P-MaNGA would not be selected in the MaNGA samples, due to their low redshift and hence low radial coverage by the MaNGA IFUs. These galaxies, p9-127A (Fig. A4) and p9-61A (Fig. 6), are observed with N_{127} and N_{61} IFUs, cover 0.7 and 1.2 R_e, and are visually identified as a face-on spiral and an early-type galaxy, respectively. The high number of fibres per unit radius means that we are able to derive more detailed, but radially limited, data than would be achievable with the full MaNGA samples.

As an example, galaxy p9-61A shows in its population maps and gradients a nearly flat metallicity profile with a ring of younger metallicities around the young central core. Its older population is shown as a 4 Gyr ring in $\langle \log age\rangle_L$around the core before becoming younger in its halo population. This is more difficult to see in $\langle \log age\rangle_M$, suggesting that the mass fraction of young stars in the halo is small. The metallicity gradient is nearly flat on average, apart from the low-metallicity ring causing a dip in the profile. The dust lane stretching vertically is clearly recovered in the dust attenuation map. We can clearly see the effect of the dust in the age and metallicity maps too, with the dust regions corresponding to lower ages (particularly in $\langle \log age\rangle_L$, very suggestive of recent

Downloaded from https://academic.oup.com/mnras/article-abstract/449/1/328/1317763
by Haverford College user
on 15 February 2018

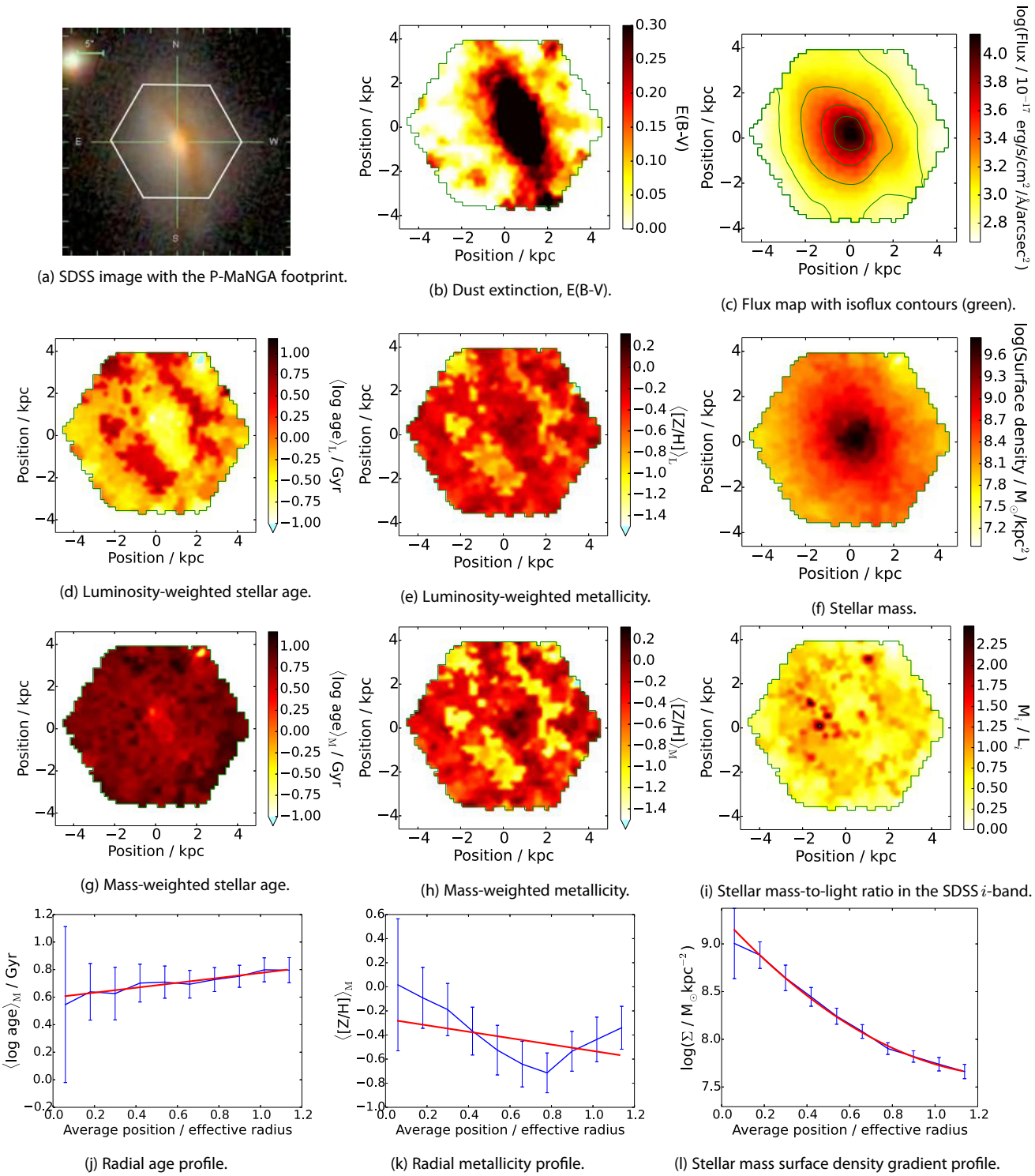

Figure 6. Group β, galaxy p9-61A as in Table 2. Stellar population maps and profiles analysed using MILES-based models with their full parameter range, as described in detail in Fig. 5. Observed under the same setup as galaxy p9-19B (Fig. 5), except with an N_{61} IFU, and observed to a higher spatial resolution than would be targeted for the MaNGA sample.

star formation or a continuous star formation history) and higher metallicities.

The high spatial detail in these two cases will not be possible to recover in MaNGA due to the higher redshift, and therefore lower spatial resolution of the target galaxies. None the less, the radial profiles are similar in the range of errors to the group α primary galaxies, with 0.04, 0.11 dex in age, 0.05, 0.19 dex in metallicity and 0.03, 008 dex in surface mass density profiles for p9-127A and p9-61A, respectively. Due to the smaller radial extent probed (0.7 and 1.2 R_e), this gives somewhat higher errors on the gradients recovered of 0.07, 0.13 dex/$R_e$in age and 0.09, 0.18 dex/$R_e$in metallicity, for p9-127A and p9-61A, respectively.

Downloaded from https://academic.oup.com/mnras/article-abstract/449/1/328/1317763
by Haverford College user
on 15 February 2018

4.3 MaNGA-selected galaxies with lower quality data: Group γ

Five galaxies fall into the category of being selected in MaNGA, but due to testing of the P-MaNGA instrument, have lower exposure times, and/or were taken in poor observational conditions. Specifically, plate 11 and plate 4 have one and two hour exposure times, respectively, compared to the MaNGA exposure time of three hours, and plate 11 has the additional problem of having been observing under an airmass of 1.5, see Table 2.

We begin by looking at plate 4, which has observational conditions somewhat closer to what can be expected from the MaNGA sample than plate 11. Galaxies p4-19B (Fig. A5) and p4-19C (Fig. 7) would fall in the primary MaNGA sample, with N_{19} IFU coverage of 1.4 and 1.3 R_e, respectively. We take galaxy p4-19C as an example of galaxies in this group. It is an early-type galaxy, that from the stellar age population map has an intermediate-age (6 Gyr in both $\langle \log \mathrm{age} \rangle_L$and $\langle \log \mathrm{age} \rangle_M$) core with a very flat gradient out to large radii. The $\langle [Z/H] \rangle_L$ and $\langle [Z/H] \rangle_M$ map shows a clear negative gradient; going from approximately half-solar metallicity to $[Z/H] = -0.5$. The stellar mass density map is relatively smooth and radially symmetric.

The poorer exposure times results in somewhat poorer stellar population radial recovery than the group α and β galaxies. Errors are of the order of 0.06, 0.09 dex in age, 0.10, 0.21 dex in metallicity, and 0.06, 0.09 in stellar mass density for the profiles of p4-19C and p4-19B, respectively. Stellar mass density profile errors are the least affected compared to group α which suggests that the quality of data lost by the lower exposure time affects age and metallicity determinations more significantly than surface mass density determinations. The corresponding respective errors on the gradients are 0.07, 0.11 dex/R_e in age and 0.08–0.21 dex/R_e in metallicity on average. Thus, a 2 h exposure, whilst giving about a factor 1.5 higher in error on the radial information obtained compared to MaNGA-like 3 h exposures, can still give significant age gradients for many galaxies but would not be able to significantly test many metallicity gradients.

Plate 11 has two galaxies that would be selected in MaNGA, p11-61A and p11-19B, in the primary and secondary samples, respectively. We do not show their stellar population maps since they represent much poorer data quality than what we expect from MaNGA, and the high pixel-to-pixel variance of the maps make them difficult to interpret. Instead, we describe them briefly here.

Galaxy p11-61A is visually identifiable as an inclined disc galaxy, with N_{61} IFU coverage of 1.5 R_e, with a red core with bluer surroundings. This is matched to an older ($\langle \log \mathrm{age} \rangle_L = 5$ Gyr/$\langle \log \mathrm{age} \rangle_M = 10$ Gyr compared to surrounding $\langle \log \mathrm{age} \rangle_L = 0.5$ Gyr/$\langle \log \mathrm{age} \rangle_M = 3$ Gyr, metal-rich ($\langle [Z/H] \rangle_M = 0.2$ dex compared to -0.1 dex surroundings) bulge with a 1 kpc radial size, giving a strong negative age gradient. However, the stellar population maps and particularly the dust attenuation map shows a high degree of scatter that is not spatially confined to a particular region, suggesting that we are suffering from the effects of poor observational conditions.

Similarly, galaxy p11-19B, a face-on blue spiral galaxy, shows a high degree of scatter in its stellar population maps, particularly in its age map. This galaxy has an average age of 500 Myr, and also has a 2-Gyr red component in the south at the same redshift as the central galaxy visible in the SDSS image.

The stellar population radial profile recovery is somewhat better in p11-61A, despite both showing signs in their maps of artificial irregularity in their age and metallicities resulting from uncertainty in the spectral fit. This could be the result of galaxy p11-61A being a highly compact object compared to every other object in the sample and thus its fluxes on each individual fibre being higher. Since this galaxy is therefore a much brighter per unit area than other galaxies in the sample we expect errors on its gradients to be lower than the other galaxy in this sub-sample, p11-19B.

The radial profile errors are 0.09, 0.27 dex in age, 0.11, 0.36 dex in metallicity and 0.07, 0.16 dex in stellar mass density for p11-61A and p11-19B, respectively. We note that galaxy p11-19B has a much larger radial extent than other galaxies in the sample, which could explain the larger errors on the profile, but reduces errors in the gradients. Errors on the gradients are 0.07, 0.16 dex in age and 0.11, 0.36 dex for p11-61A and p11-19B, respectively.

4.4 Non-MaNGA galaxies with low-quality data: Group δ

This group has the highest membership of any of the identified groups above, containing seven galaxies, four in plate 11 and three in plate 4. The galaxies in this sub-sample are: p11-127A, p11-127B, p11-19A, p11-19C, p4-127A, p4-127B, and p4-61A. Rather than describing each galaxy in detail, we discuss some interesting features from this group. We later discuss the errors on the radial profiles for these galaxies as part of the sample as a whole and so refer the reader to Section 5.3 for this discussion.

A feature common to p4-127A and p11-127A is the presence of a very strong dust lane across a large portion of the observation. In both cases, this feature is shown clearly in the dust attenuation maps (Figs 8a and b for p4-127A and p11-127A, respectively) and corresponds to somewhat younger ages and less metal-rich (approximately $\langle \log \mathrm{age} \rangle_L = 3$ Gyr younger and $\langle [Z/H] \rangle_L = 0.2$ dex less compared to surroundings). Both of these cases give a clear interpretation of a dusty disc that has undergone more recent star formation than its surroundings. We also note that p11-127A has more variance in its derived stellar population properties, giving a 'speckled' appearance in the maps, compared to p4-127A, which can be attributed to the poorer observational conditions in the former case.

The observational conditions combined with the N_{19} IFU for galaxies p11-19A and p11-19C render the interpretation of stellar population maps (such as the age maps in Figs 9a and b) very difficult; however, one can draw comparisons with the qualitatively similar galaxies in the higher quality sub-samples, galaxies p4-127A and p4-19A, respectively. This gives an idea of the conclusions one might be able to draw from these galaxies if they were observed under better conditions, and conversely how and how much conclusions get blurred by observing galaxies in poor conditions. The variance of stellar population parameters of p11-19A and p11-19C additionally translates to poor constraints on these galaxies' radial profiles, and so this is a clear limitation of using such low (1 h) exposure times under poor observational conditions.

The main effect of the poor observational conditions is the added Voronoi cell-to-cell variance which washes out smaller scale structure. The identification of galaxy features such as disc structure is not possible in these cases.

5 RESULTS

5.1 Radial gradients

The age and metallicity gradients for the prototype data set are summarized in the histograms of Fig. 10. We re-iterate from the beginning of this section that all gradients and radial profiles are

Downloaded from https://academic.oup.com/mnras/article-abstract/449/1/328/1317763
by Haverford College user
on 15 February 2018

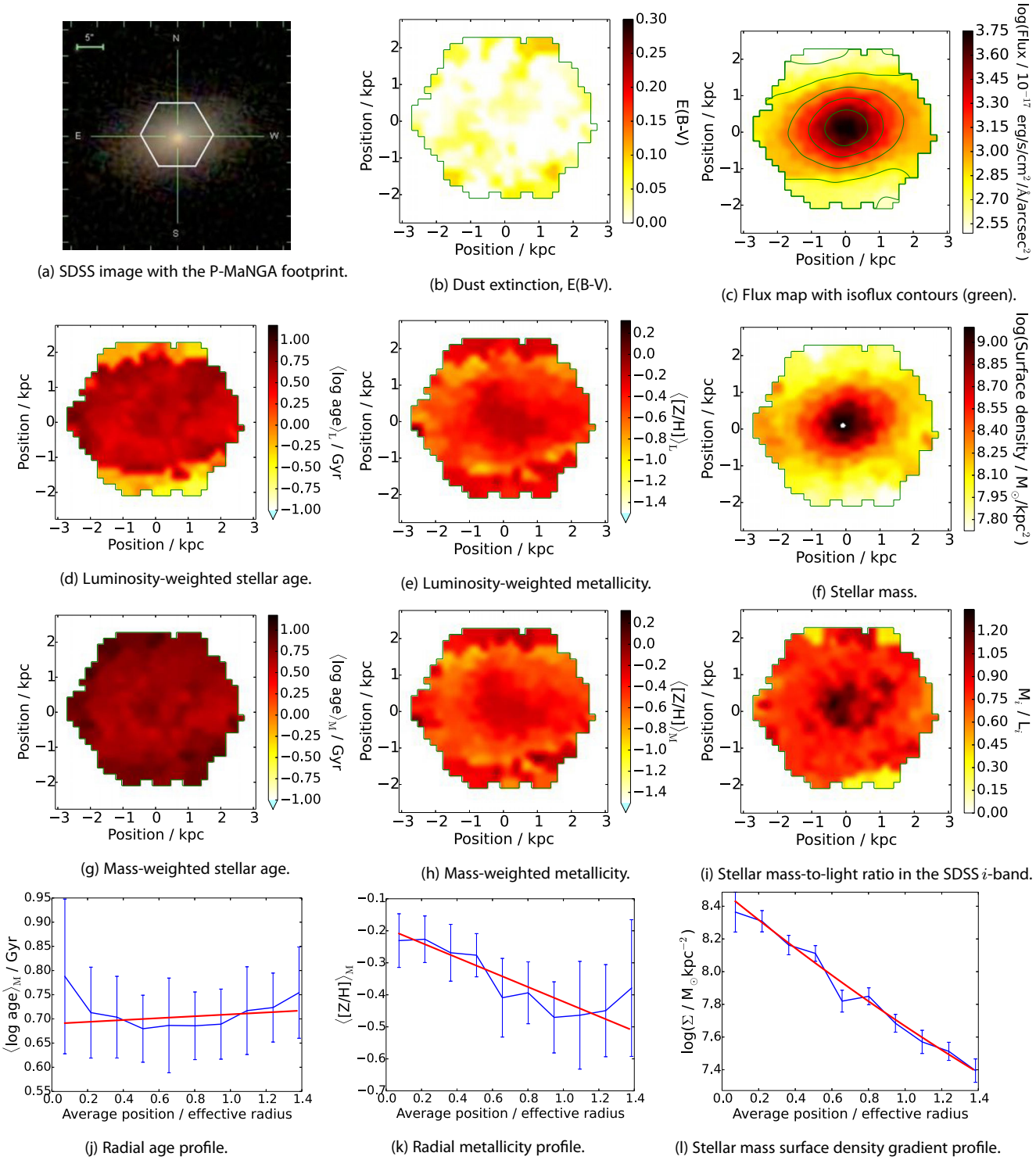

Figure 7. Group γ, galaxy p4-19C as in Table 2. Stellar population maps and profiles analysed using MILES-based models with their full parameter range, as described in detail in Fig. 5. This galaxy has been observed under poorer conditions and a lower exposure and dithering setup than expected for MaNGA. None the less, we recover a simple and smooth stellar population structure with negative age and metallicity gradients.

calculated from mass-weighted stellar population properties rather than light-weighted properties, since these more precisely trace the evolutionary history of the galaxies observed, and thus are more appropriate for assessing formation and evolutionary mechanisms.

Both age and metallicity gradients seem to draw from different distributions for spheroid/early-type galaxies and disc/late-type galaxies. Age gradients for late-types have an overall strongly negative with a mean of −0.39 dex and a wide standard deviation of 0.36 dex, compared to early-type galaxies which have a flat (mean −0.05) age gradient and 0.24 dex standard deviation. Conversely, metallicity gradients for late-type galaxies are flat (mean 0.00 dex), with 0.17 dex standard deviation, and early-type galaxies have a

Downloaded from https://academic.oup.com/mnras/article-abstract/449/1/328/1317763
by Haverford College user
on 15 February 2018

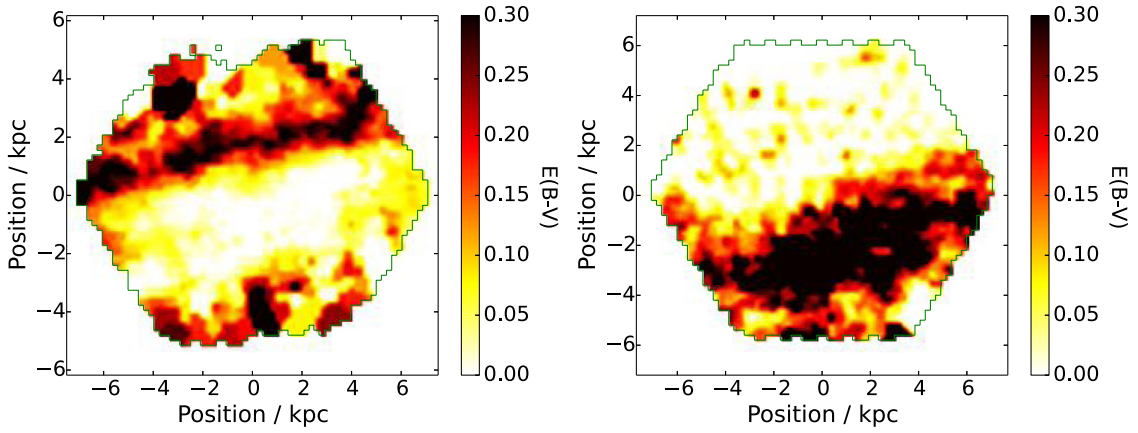

(a) Dust attenuation map of galaxy p4-127A.

(b) Dust attenuation map of galaxy p11-127A.

Figure 8. Group δ galaxies p4-127A and p11-127A as in Table 2. These two galaxies have very clear dust lanes that show evidence of more recent star formation than their surroundings. Both of these galaxies have been observed under poorer conditions and lower exposures and dithering setup than expected for MaNGA, although p4-127A has been observed under worse conditions and setup than p11-127A, translating to a more speckled appearance in its maps.

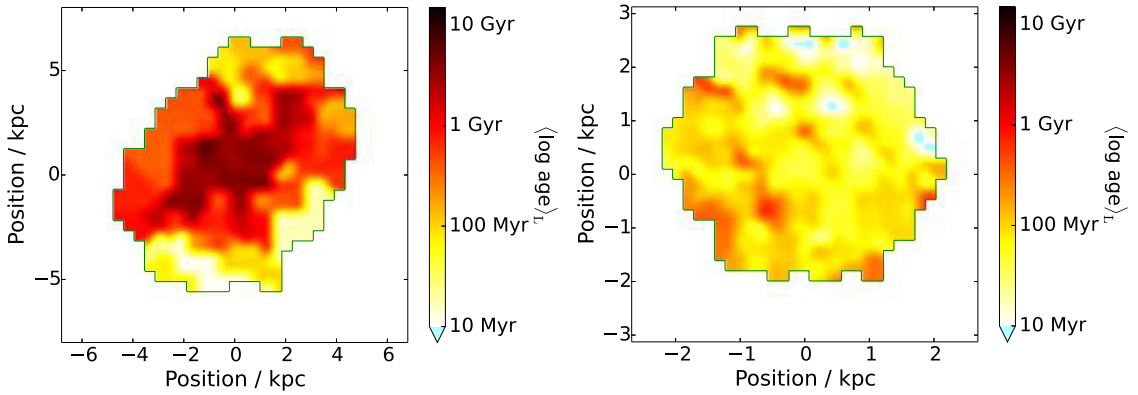

(a) Light-weighted stellar age map of galaxy p11-19A.

(b) Light-weighted stellar age map of galaxy p11-19C.

Figure 9. Group δ galaxies p11-19A and p11-19C as in Table 2. These galaxies have been observed under much poorer conditions and much lower exposures and dithering setup than expected for MaNGA. Both of their maps show an unclear distribution of stellar population properties, with in general high amounts of variance between neighbouring pixels.

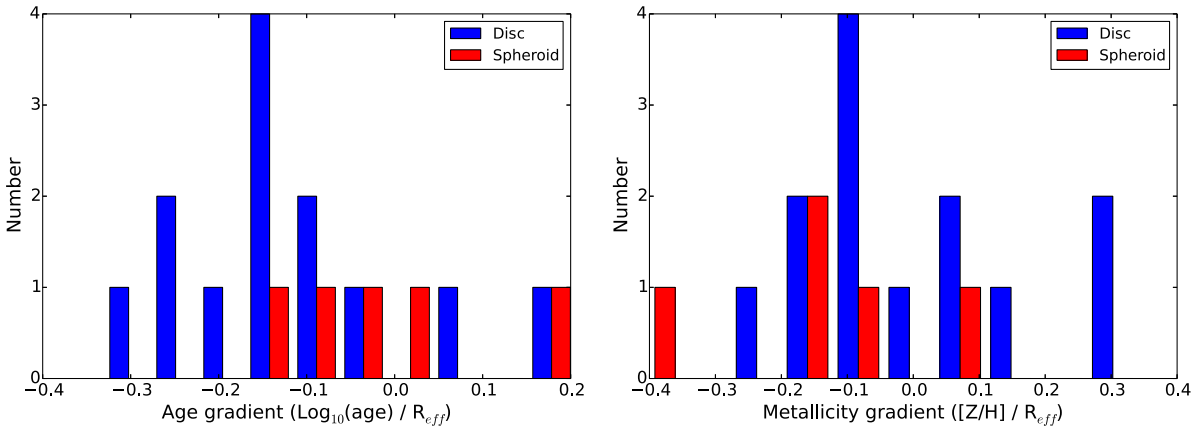

Figure 10. Summary of all of the age (left) and metallicity (right) gradients deduced for the P-MaNGA data set, using visual morphological classification from SDSS imaging data.

Downloaded from https://academic.oup.com/mnras/article-abstract/449/1/328/1317763
by Haverford College user
on 15 February 2018

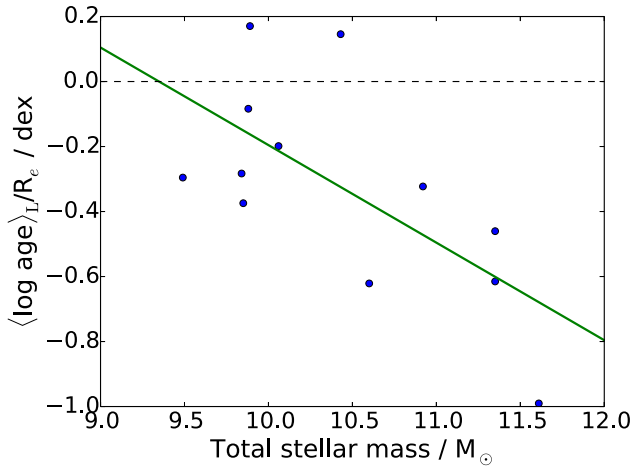

Figure 11. A scatterplot showing the relation between photometric stellar masses and $\langle \log \mathrm{age} \rangle_\mathrm{L}$ as derived in this paper, for the late-type galaxies in the P-MaNGA sample as listed in Table 2. This relation is plotted in order to compare to the conclusions of González Delgado et al. (2014, see text). In dashed black, we show zero gradient line, and in green we show a linear regression line.

negative gradient of mean −0.15 dex with a 0.14 dex standard deviation.

Our findings on metallicity and age gradients agree very well with previous analyses of early-type galaxies, such as in Kobayashi & Arimoto (1999), Saglia et al. (2000), Tamura et al. (2000), Mehlert et al. (2003), Wu et al. (2005), Annibali et al. (2007), Sánchez-Blázquez et al. (2007), Rawle et al. (2008), and Kuntschner et al. (2010), in particular the lack of a significant age gradient in early-type galaxies.

For our late-type galaxy sample, we do not attempt to separate the light from the bulge and from the disc as it is beyond the scope of this work. Thus, our overall gradients, particularly in age, cannot be compared directly to previous work that has done this, for example Sánchez-Blázquez et al. (2014) and MacArthur, González & Courteau (2009), and work based on local galaxies such as Williams et al. (2009) and Barker et al. (2007). However, we note that our metallicity gradient estimates agree well in these cases. In this paper, we conclude that bulge–disc separation is the main driver for the negative age gradients seen in P-MaNGA galaxies and so our conclusions agree well with the literature. For previous work assessing the age and metallicity gradients of late-type galaxies including the disc and bulge, such as Sánchez-Blázquez et al. (2011) and Yoachim & Dalcanton (2008), we find good agreement with our gradients and overall conclusions.

With our limited sample size, we cannot draw significant conclusions on the relationships of stellar population gradients as a function of other physical properties. However, in Fig. 11, to compare with recent work by González Delgado et al. (2014) we plot total stellar mass as measured in P-MaNGA against $\langle \log \mathrm{age} \rangle_\mathrm{L}$ for the late-type galaxies to see if our results are consistent. Total stellar mass estimates are calculated from *u*, *g*, *r*, *i*, *z* photometry following the method in Maraston et al. (2006, 2013) for SDSS-III/BOSS galaxies (Pforr et al., in preparation). 'Photometric' stellar masses do not suffer from aperture effects as will be described in Section 5.4. In Section 5.4, we also test the relationships between gradients and total stellar mass.

We find that at low masses, below $\sim 10^{10}$ $\mathrm{M}_\odot$, $\langle \log \mathrm{age} \rangle_\mathrm{L}$ gradients are generally close to flat, but that above $\sim 10^{10.5}$ $\mathrm{M}_\odot$ the $\langle \log \mathrm{age} \rangle_\mathrm{L}$ gradients are very strongly negative. This matches well with González Delgado et al. (2014), who find that low-mass disc galaxies show flat age gradients but at higher masses the gradients become strongly negative. They also test early-type galaxies but with our very small sample, we are unable to see a clear correlation with total stellar mass. In our sample, we find no clear evidence for relationships between $\langle \log \mathrm{age} \rangle_\mathrm{M}$, $\langle [\mathrm{Z/H}] \rangle_\mathrm{L}$ or $\langle [\mathrm{Z/H}] \rangle_\mathrm{M}$ with total stellar mass, suggesting that the main driver for the $\langle \log \mathrm{age} \rangle_\mathrm{L}$–$\mathrm{M}_\odot$ relation is the radial transition between bulge and recent star formation in the disc.

5.2 Beam smearing

Results from IFU experiments can be threatened by the risk of 'beam smearing', an effect that spreads out the signal for a given pixel position into nearby pixels. Beam smearing is the combination of three observational effects: atmospheric point spread function, sampling size of the IFU fibres, and dithering; the process of offsetting the telescope from the target by small amounts such that the fibres collectively observe whole footprint, including gaps between fibres. The effect of beam smearing should be greatest for the smaller IFUs.

Given that our largest sample of galaxies are late-type galaxies and these have generally a large range of negative gradients, we can test to see if decreasing the IFU size results in poorer age gradient recovery, for these galaxies. Metallicity gradients are not tested since there are both positive and negative gradients in the late-type sample which may be hard to separate between, and our early-type sample is too small to derive meaningful conclusions in this area.

In Fig. 12, we plot the age gradient histograms for the late-type galaxies shown in Fig. 10, but as a function of IFU size: N_{19}, N_{61}, and N_{127} fibre IFUs. In the left-panel we, plot the mass-weighted radial age gradients as we have plotted in Fig. 10, where we find no correlation between mean gradient and IFU size. The mean age gradients are −0.12, −0.19, and −0.13 dex for N_{19}, N_{61}, and N_{127} observations, respectively.

We also plot light-weighted age gradients for comparison in the right-hand panel, since these will be more sensitive to bright stellar populations and so should be more directly related to beam smearing effects. We therefore expect larger (in magnitude) gradients to be present since small amounts of star formation in an otherwise more passive galaxy can cause large changes in the light-weighted profiles. In this case, the separation is much easier to see, with N_{19} observations giving much flatter gradients (mean −0.08 dex) than N_{127} observations (mean −0.55 dex), and N_{61} lying in between but closer to the N_{127} observations (mean −0.43 dex). We note that the two galaxies with the largest negative age gradients, around -1.0 $\langle \log \mathrm{age} \rangle_\mathrm{L}/R_\mathrm{e}$, correspond to two late-type galaxies with both spiral or disc features and very prominent bulges, p9-127A and p11-127A, clearly identifiable visually and covered within P-MaNGA N_{127} footprint. Hence, it is expected that these galaxies should have very large negative age gradients in their light-weighted profiles, compared to other types of galaxies or smaller IFU sizes where the morphological features may be more difficult to separate.

We therefore conclude that beam smearing does appear to affect the lowest IFU sizes much more in the light-weighted properties, and thus is more sensitive to bright stellar populations such as from very young stars, but this effect is mitigated by calculating mass-weighted properties.

We do not go further to quantify this effect due to small sample size, and thus overlap with other effects such as radial extent and other physical galaxy properties. A detailed analysis of N_{127}

Downloaded from https://academic.oup.com/mnras/article-abstract/449/1/328/1317763
by Haverford College user
on 15 February 2018

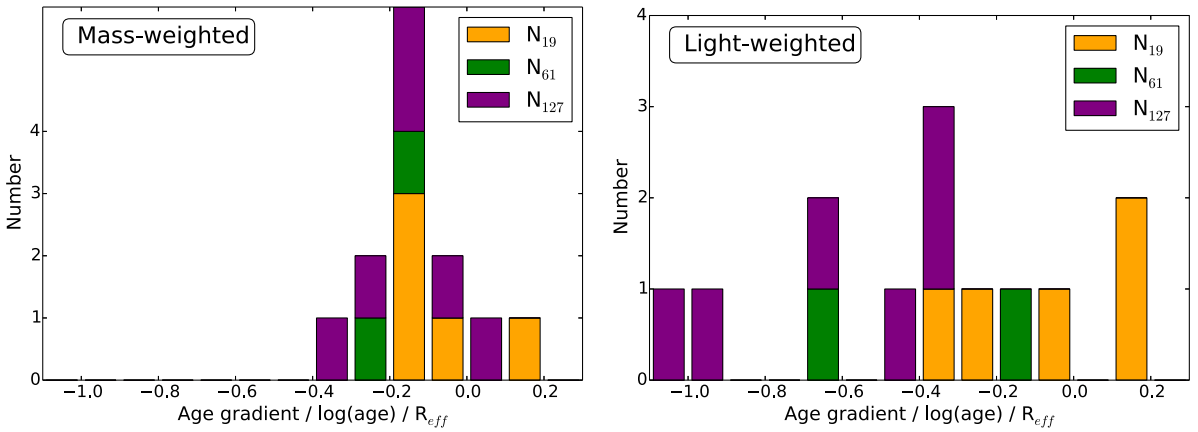

Figure 12. Histograms of age gradients as in Fig. 10, selecting only the late-type galaxies in the sample, but as a function of IFU size. In the left-hand panel, we show mass-weighted age gradients as in the other profile and gradient figures in this paper. In the right-hand panel, we show light-weighted age gradients since these will trace bright stellar populations, and thus are important for testing the effect of beam smearing.

MaNGA data, downgraded to the other IFU sizes, will be necessary for robust quantification, which will be subject of future work once a larger sample is available. Additionally with the much larger MaNGA sample, we will be able to carry out this analysis with comparable inclinations, morphologies, and colour gradients.

5.3 Statistical error as a function of observational conditions

In each of the P-MaNGA galaxies analysed, we have derived stellar population property statistical errors on each of their pixels, as described in Section 3, which we then propagate to standard errors on each of the elliptical bins in the radial profiles. We explore how these errors vary as a function of the observation conditions and setup used to observe each galaxy.

To measure the error on the gradient, we need to find the standard error at the median radial bin. However, this decreases as a function of the number of pixels used increases, and does not include the covariance between pixels, thereby underestimating the uncertainty on the fit. In this work, we do not estimate covariance between pixels due to the prototype nature of the observations. To compare these errors across each of the P-MaNGA galaxy, we therefore take the standard deviation averaged across all the pixels at each radial bin, assume the number of independent observations is equal to the number of grid points analysed divided by 16, as explained in Section 3.2, and find the median of this value. To be concise, we shall refer to this as the *median standard error*. This value remains constant as the number of pixels in each bin is changed, allowing us to compare this value across each galaxy directly.

Corresponding errors on the gradients are calculated from the errors on the profile points by using bootstrap resampling of 10 000 points for each profile point recovered and recalculating the linear gradient on each resample. We note that the error calculated assumes a linear fit, hence does not describe *how linear* the radial profiles are. We assume that the errors on each point are Gaussian, which typically is an accurate approximation of the error obtained from the spectral fit with FIREFLY. We note that errors on the gradient will not directly correspond to the errors on the profile since each galaxy is observed with a different radial extent.

The upper panel of Fig. 13 presents the median standard error for mass-weighted stellar age, metallicity, and surface mass density as a function of plate, each of which corresponds to a set of observational

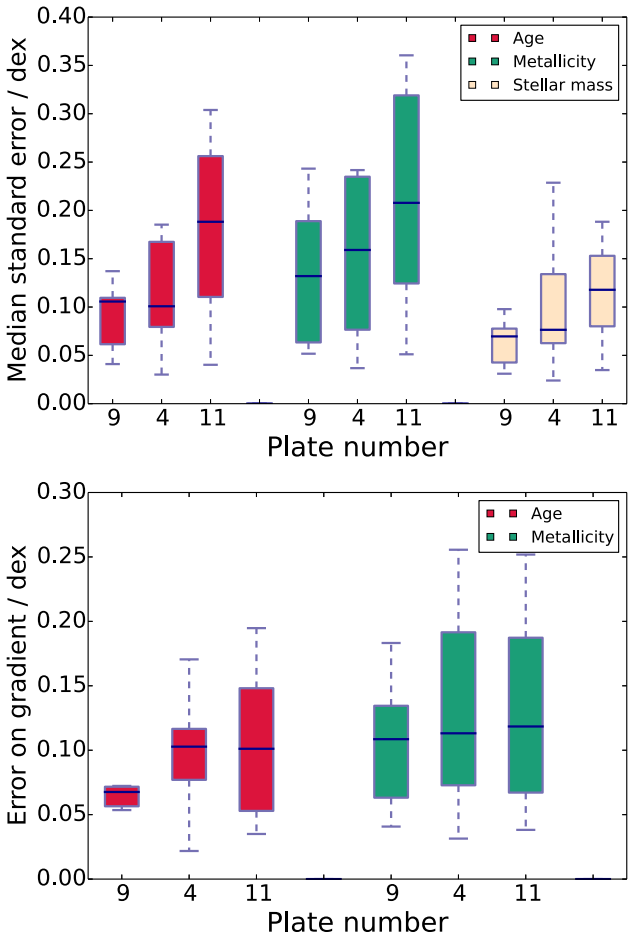

Figure 13. Median standard errors (top panel), and errors in the linear gradient (bottom panel), of stellar population profiles as a function of property and observational conditions grouped by plate number, see Table 5. Errors in the gradient are calculated through bootstrap resampling of the median standard errors. Each box plot shows the median and interquartile range of the corresponding sub-sample, each of which contains the median standard error and the errors on the gradients of six galaxies. Stellar mass density gradients not shown as they are not appropriate to fit with a linear profile.

Downloaded from https://academic.oup.com/mnras/article-abstract/449/1/328/1317763
by Haverford College user
on 15 February 2018

Table 5. Summary of errors on radial profiles and gradients as a function of observational conditions and setup.

Field	Groups	Conditions and setup	Median error in profile/dex			Error on gradient/dex/R_e	
			Age	Metallicity	Mass density	Age	Metallicity
9	α/β	Exposure 3.0 hr, seeing 1.7 arcsec	0.10	0.13	0.07	0.07	0.11
4	γ/δ	Exposure 2.0 hr, seeing 1.3 arcsec	0.10	0.16	0.08	0.10	0.12
11	γ/δ	Exposure 1.0 hr, seeing 2.0 arcsec, (airmass ∼1.5)	0.19	0.22	0.12	0.10	0.12

conditions summarized in Table 4. We can clearly see that for all three properties, plate 9 provides the smallest errors, and plate 11 provides the highest errors, on the radial profiles. Each box plot has a high interquartile range due to the small sample size, as there are only six galaxies in each bin. We remind the reader that only plate 9 has been observed with MaNGA-quality conditions and setup (3 h exposure), whereas plate 4 and plate 11 have less than MaNGA-quality observations (2 h exposure, and 1 h exposure with 1.5 airmass, respectively).

The corresponding errors on the age and metallicity gradients are shown in the lower panel, also summarized in Table 4. We note that this panel does not linearly relate to the upper panel due to each of the galaxies having different radial extents, as well as some parts of the profile being more important than others to constrain the errors on the gradient. We do not calculate stellar mass density gradients as they are not appropriate to fit with a linear profile. Again, plate 9 provides the best gradient determination, with the smallest interquartile ranges in the gradient errors. We thus deduce that plate 9 galaxies provide a more stable and reliable gradient determination for both age and metallicity. There is less evidence to separate plate 4 and plate 11 galaxies in this case, other than plate 11's age gradients seeming to have a larger interquartile range and thus provides the least stable errors estimations as a function of galaxy observed. Metallicity gradients show little separation in their median value for all three plates, despite plate 9 having a lower interquartile range, suggesting that *average* metallicity gradients are on average less sensitive to observational quality than age gradients but do become less stable with each galaxy, with worsening observations. Due to the small size of P-MaNGA's sample, we do not further separate on galaxy type, radial extent, or suggest stronger conclusions on the errors on the profiles and gradients. We summarize the errors in Table 5.

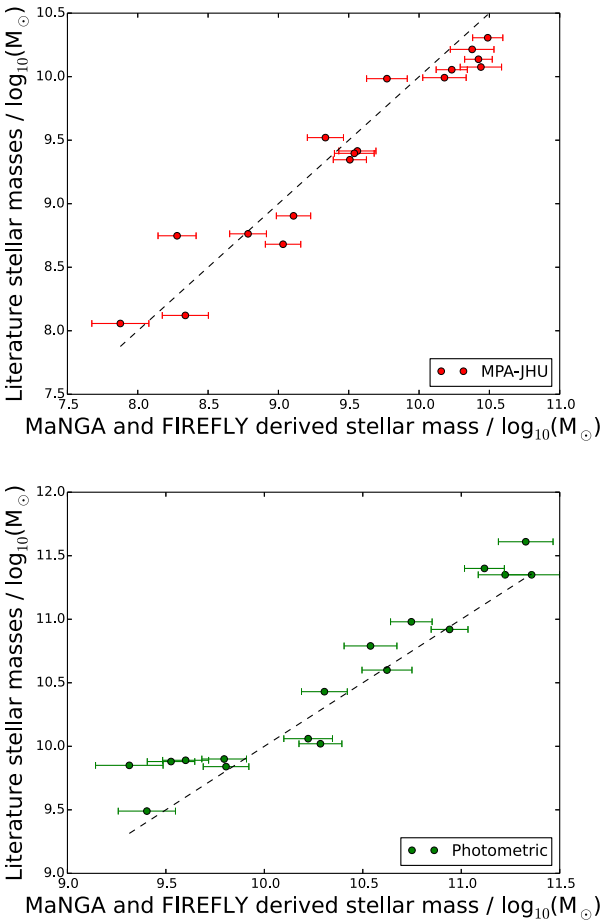

Figure 14. A comparison of the total stellar mass derived for each of the P-MaNGA galaxies between this work, the MPA-JHU catalogue in the SDSS Data Release 8 pipeline, and the 'Photometric'-based stellar masses based on Pforr et al. (2012). In black, we show a one-to-one dashed line. We note that the two panels have different scales due to using a 3 arcsec aperture in the MPA-JHU comparison, but the full P-MaNGA aperture in the photometric comparison.

5.4 Stellar mass estimates

Given that our full spectral fitting also allows the calculation of stellar masses, we make a qualitative comparison with previous estimates for the P-MaNGA galaxies.

First, we compare to the widely used MPA-JHU catalogue of the SDSS Data Release 8 pipeline (see Table 2) in Fig. 14. These masses are based on broad-band *ugriz*-filter SED fitting scaled to 3-arcsec fibre sizes. This spatial coverage is much smaller than our P-MaNGA, which extends up to 1.5 effective radii. Hence, we integrate the surface mass density only up to this radius for each galaxy. We find good overall agreement with the MPA-JHU masses with a systematic offset of about 0.1 dex and a scatter of 0.2 dex.

We note that the presence of galaxy gradients may complicate this simple scaling of the M/L ratio as this quantity depends on both age and metallicity. In addition, the stellar population modelling and fitting technique is different. The MPA-JHU masses are based on Bruzual & Charlot (2003) stellar population models and a coarser grid of ages than this work, using (unpublished) models based on the MILES stellar library and a Kroupa IMF. Hence, the stellar library and most importantly the IMF are the same, but the population models and age grids used are different. Other effects could also introduce systematics. The subtraction of stellar mass loss which is performed in our modelling, may correspond to 30–40 per cent by mass depending on the IMF (see Maraston 1998, 2005) and it is not clear to us whether and how this is accounted for in the MPA-JHU calculations.

Furthermore, masses obtained via spectral fitting may be different from those from broad-band SED fit particularly when the former refer to low S/N spectra. Maraston et al. (2013, see the appendix) find that the stellar mass of SDSS-III/BOSS galaxies at redshift 0.4–0.6 were smaller when computed via broad-band *ugriz* SED fitting

Downloaded from https://academic.oup.com/mnras/article-abstract/449/1/328/1317763
by Haverford College user
on 15 February 2018

by 0.25 dex compared to those obtained via PCA spectral fitting by Chen et al. (2012). The hypothesis is that the spectral fitting of low S/N spectra may lead to high ages, which have higher M/L ratios. Chen et al. (2012) quantify this effect by applying full spectral fitting to high S/N empirical spectra and conclude in this direction. In Wilkinson & Maraston (in preparation), we try to quantify this effect via mock galaxies with known input M^*.

This source of systematics is in common with the second stellar mass comparison plot in Fig. 14, namely 'photometric'-based stellar masses calculated with the same model and fitting set up as those output of the SDSS-III/BOSS data release and pipeline (Dawson et al. 2013). In brief, these are also broad-band *ugriz* SED fitting performed with the publicly available code HYPER-Z customed with Maraston (2005) models, Kroupa IMF, and our same account of mass-loss. The template star formation histories encompass a range of exponentially declining τ-models, ranging from 0.1 to 3 Gyr. No dust reddening is applied to the fitting in order to minimize the age–dust degeneracy which can lead to too young solutions which underestimate the true stellar mass (see Pforr et al. 2012). We note that a clump of galaxies in this lower left of the plot which seem even quite far from the line are all identified as star-forming late-type galaxies in this sample, and so we expect a τ to not be able to capture these more complex star formation histories, explaining this discrepancy. Our stellar masses are on average 0.15 dex smaller than these photometric total masses. This offset will mainly come from the difference in aperture. Since P-MaNGA covers on average 1.5 R_e rather than the full extent of the galaxy as in the photometric masses, we expect our observations to cover ∼75 per cent of the light. This would give a 0.12 dex underestimate of the stellar masses, consistent with the offset we find in our comparison.

5.5 Effect of input stellar library

As anticipated in Section 3.1, we perform spectral fitting with models based on three different empirical stellar libraries. We use the same example galaxy p9-127A for which we show in Fig. 15 $\langle \log \text{age} \rangle_L$ and $\langle \log \text{age} \rangle_M$ maps, light-weighted age, and metallicity profiles and stellar mass density profiles. In both this section and Section 5.6, we use light-weighted properties for the radial profiles, as these are more sensitive tracers of processes that we wish to test recovery of, such as recent star formation or very low metallicity stellar populations. However, we also discuss the differences between the light- and mass-weighted age maps.

Note that in this comparison we have restricted the model parameters to be identical, hence results obtained with the MILES-based models here will be different from those obtained with the full parameter range. This corresponds to a wavelength range of 3900–6800 Å, ages varying between 30 Myr and 15 Gyr, and metallicities of 0.5, 1.0, and 2.0 times solar metallicity. Hence for example, the metallicity gradient for MILES-based models is somewhat positive in this case compared to the negative gradient for the same galaxy fit with the full parameter range, for which we are able to use lower metallicity stellar population components.

These plots illustrate behaviours of the model comparisons that are found among all test galaxies, namely:

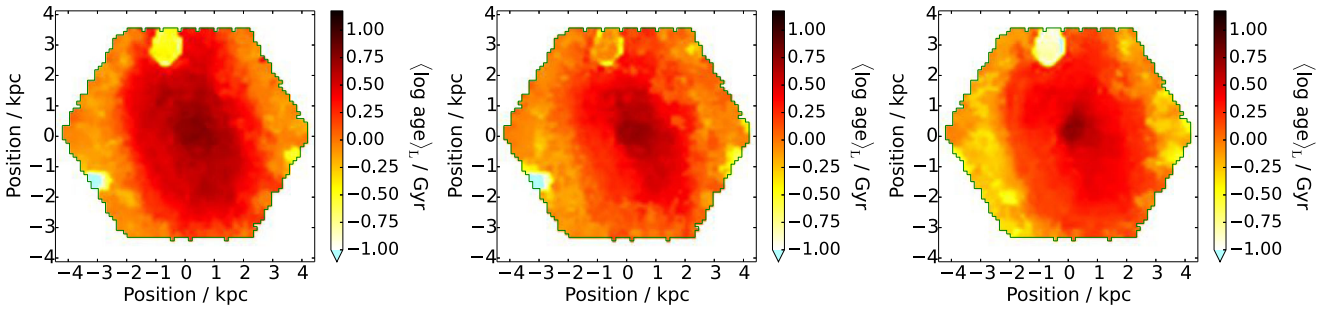

(a) Light-weighted age maps of p9-127A as a function of stellar library; MILES, STELIB, and ELODIE are shown in the left, middle, and right panels respectively.

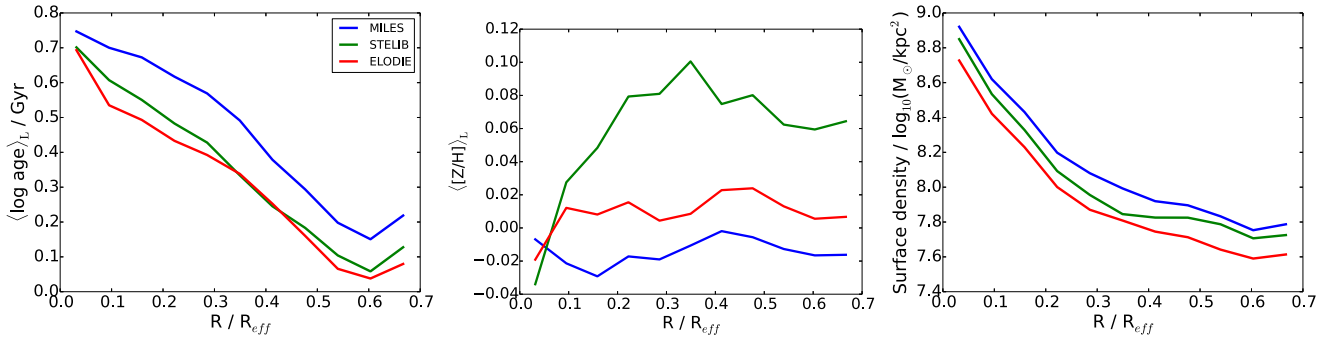

(b) Radial profiles of stellar age, metallicity and surface mass density respectively as a function of stellar library.

Figure 15. The effect on galaxy properties of the stellar library input in the stellar population model. In all cases, models were fitted with identical stellar population parameter grids (see Section 3.1). Maps are composed of Voronoi-binned cells of properties, corresponding to binned spectra that cover enough sky area such that the median S/N at any given cell is as close as possible to 5. Typically, this means that the outer Voronoi cells of the galaxy cover a more extended area than the inner cells. The radial properties are computed from spectra summed in annuli that have radial extent that approximately scales logarithmically, in order to give the surface mass density (right-hand side) profiles.

Downloaded from https://academic.oup.com/mnras/article-abstract/449/1/328/1317763
by Haverford College user
on 15 February 2018

(i) Overall distributions of stellar ages are similar in structure; however, the average age values can vary by an order of 3 Gyr in the worst cases (see for example, the radial extent of high ages in the MILES stellar age map in Fig. 15, compared to the other two models). Age gradients are the same for the three models.

(ii) Metallicity maps and profiles also show very similar structures among the three models, though STELIB-based models correspond to a slight increase of 0.1 dex in [*Z*/H] in the outer parts of its maps compared to the other models. The metallicity gradients are flat for MILES and ELODIE-based models but the STELIB-based models have a clear increase in the inner 0.2 R_e, giving a positive metallicity gradient across the whole galaxy of 0.1 dex/R_e.

(iii) We note that ELODIE-based models have slightly redder spectra than STELIB-based models at these approximate parameters, explaining why STELIB-based models fits for higher metallicity and slightly higher age. Age–metallicity degeneracy causes this colour offset to mix between age and metallicity offsets. This is visible in Fig. 15 where the larger offsets in either the age or metallicity profiles at a given radius correspond to a smaller offset in the other profile.

(iv) Stellar mass maps obtained also show very similar structure, with 0.1 dex variation between models visible in the gradients. This is interpreted as different models fitting differently according to age–metallicity degeneracy, with the older ages (as in the MILES-based models) corresponding to higher stellar mass.

These systematic effects between libraries may be important and so we provide the fitting parameters obtained for all three libraries used. These conclusions allow us to have estimates for systematic errors in the modelling to bear in mind when considering comparisons with other fitting codes, methods, models, and surveys. A more quantitative and comprehensive analysis of this will be subject of future work based on a larger set of MaNGA galaxies.

5.6 Comparison with the CALIFA galaxy survey and with PPXF

In the P-MaNGA sample, there are three galaxies that overlap with the CALIFA survey (Sánchez et al. 2012). Two of these lie in group δ, whose poor data quality in the P-MaNGA survey make a direct comparison between the results of the survey difficult to interpret. However, one galaxy, p9-127A, lies in group β, enabling a good opportunity to explore how MaNGA-like observations compare to CALIFA observations, even though this galaxy will not be in MaNGA due to its redshift being too low.

The fitting code used in CALIFA is STARLIGHT (Cid Fernandes et al. 2005), and the stellar population models are a blend of Vazdekis et al. (2010) and González Delgado et al. (2005) for STARLIGHT/CALIFA.

In the left-hand panels of Fig. 16, we plot the light-weighted stellar age and metallicity of p9-127A as measured by applying CALIFA data cubes (CALIFA 277 in Cid Fernandes et al. 2013) but with this paper's plotting scheme. These can be compared directly with the corresponding plots applying FIREFLY to P-MaNGA data cubes. We also compare to PPXF fits of the same P-MaNGA spectra as used in this paper's analysis in the middle panels of Fig. 16.

We find a remarkable agreement in the structures of maps between STARLIGHT/CALIFA and FIREFLY/P-MaNGA, particularly between the stellar age and stellar mass map. The CALIFA metallicity map appears to show much finer structure in its core than the P-MaNGA map, although the general high-metallicity core with lobes of lower metallicity is matched in both codes and surveys. This finer structure could be artificial, arising from uncertainties in deconvolving the CALIFA fibre spectra into the data cube, since CALIFA has a lower fibre density across the P-MaNGA radial footprint analysed in this galaxy.

We look quantitatively at these differences by binning the properties in elliptical annuli in the right-hand panels of Fig. 16, where we have plotted the corresponding properties from the left-hand panel as radial profiles. Again, we note remarkable agreement in stellar age (<0.1 dex at all points), bearing in mind that the statistical errors plotted will be much lower than the systematic errors from flux calibration, covariance between pixels, and stellar population model uncertainties. We find a more complex structure, and generally lower values, in metallicity in the CALIFA profile than the P-MaNGA profile, differing by up to 0.1 dex in [*Z*/H]. We note that the stronger transition between high and low metallicity identified in FIREFLY and, as discussed below, in PPXF, is consistent with the bulge/disc separation visible in the SDSS image of the galaxy. The agreement here is very encouraging since we use a different set of models, base stellar population components, wavelength range, fitting code, and survey compared to Cid Fernandes et al. (2013).

In the middle panels of Fig. 16, we show the $\langle \log \mathrm{age} \rangle_L$ and $\langle [Z/H] \rangle_L$ maps extracted with the full-spectrum fitting PPXF code on the same spectra fitted with FIREFLY. For this comparison, PPXF used as input a grid of SSP models from Vazdekis et al. (2010), based on the MILES stellar library. Ages were sampled with 24 models logarithmically spaced between 0.08 and 14 Gyr, while for each age metallicity was samples by six models with [*M*/H] = [−1.71, −1.31, −0.71, −0.40, 0.00, 0.22], for a total of 144 model templates. The fit was restricted to the wavelength range from 3600 to 7400 Å. To suppress the noise in the inferred population parameter, we used linear regularization (keyword REGUL in PPXF) in the two-dimensional age and metallicity distribution. The level of regularization was chosen in such a way that the χ^2 of the regularized fit increases by $\Delta\chi^2 \approx \sqrt{2N_{\mathrm{pix}}}$ from the unregularized best-fitting χ^2. This provides the smoothest age–metallicity distribution consistent with the observed spectrum. The results are very weakly sensitive to the choice of the regularization parameter. The stellar kinematics was fitted simultaneously to the stellar population. We adopted a six-degree multiplicative polynomial to account for possible inaccuracies in the relative flux calibration and remove the effect of dust attenuation on the continuum shape. No additive polynomials were used to avoid affecting the line strength of the SSP models.

The profiles and maps of PPXF fits find good spatial agreement with FIREFLY. The systematically higher ages, by about 0.2 going out to 0.4 dex, and the greater smoothness of the age maps compared to both STARLIGHT/CALIFA and FIREFLY/P-MaNGA could arise from differences in the ages of the SSP templates used. For example, the other two codes include younger ages (in our case down to 6.5 Myr, see Table 3). The metallicity of the PPXF fits agrees with the other codes to within 0.1 dex. This suggests that the greatest sensitivity on the results obtained is from the range of SSPs used, based on this example. We will investigate these differences in detail for a larger sample in future work.

In conclusion, we find an overall good, ∼0.1 dex, agreement between the CALIFA/STARLIGHT and P-MaNGA/FIREFLY, and across all three cases consistent recovery of the spatial features of the galaxy observed, and higher differences in age are present when comparing with P-MaNGA/PPXF which may just come by construction. Matching general profiles are recovered in all three cases, but differences caused by the different analysis codes, stellar population templates used, and models are significant and larger than the random errors in the analysis of detailed features.

Downloaded from https://academic.oup.com/mnras/article-abstract/449/1/328/1317763
by Haverford College user
on 15 February 2018

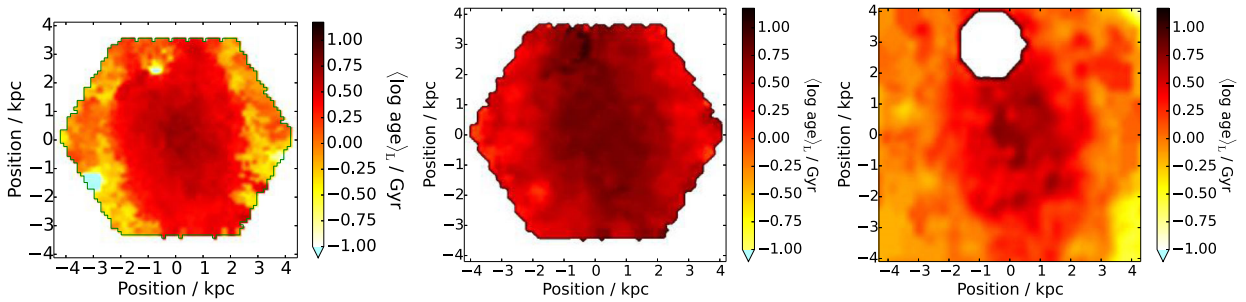

(a) Stellar age maps for CALIFA 277 / p9-127A. In the left panel are the results from this paper. In the middle panel are the results from fitting to P-MaNGA with PPXF. In the right panel, results from fitting CALIFA data with STARLIGHT are shown as derived in Cid Fernandes et al. (2013).

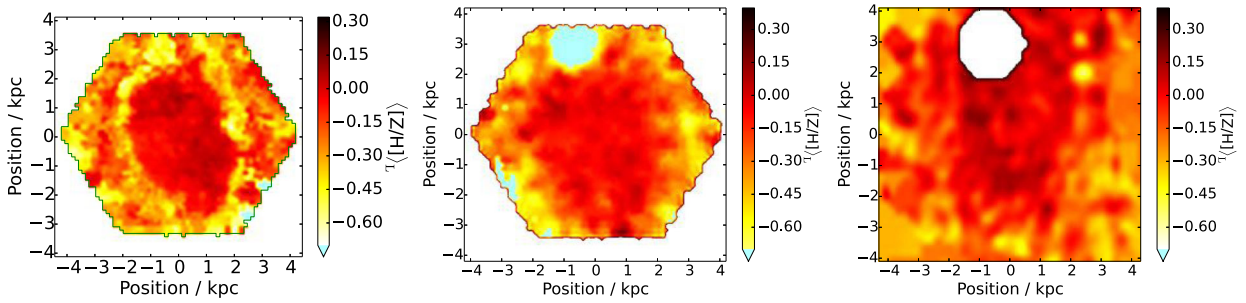

(b) As above but for metallicity.

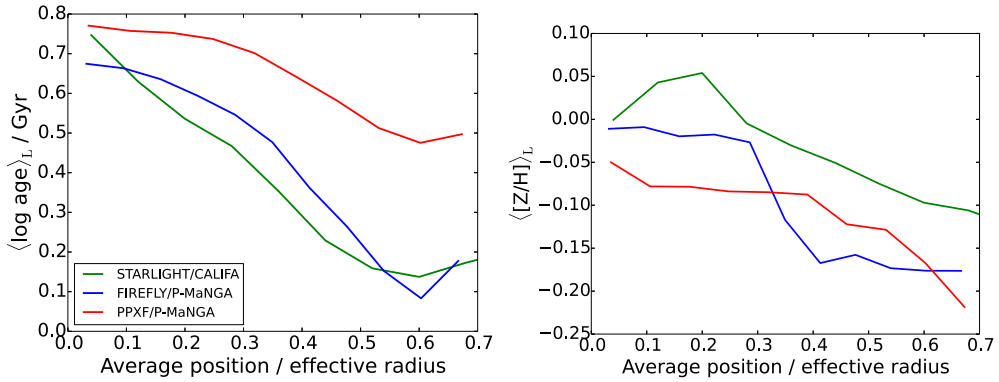

(c) Radial profiles of age (left-hand panel) and metallicity (right-hand panel), colour-coded by the survey and fitting code used.

Figure 16. Derived stellar population maps and profiles for CALIFA-277, known in this paper as p9-127A, a target shared by both the P-MaNGA and CALIFA surveys at observational conditions similar to those expected for MaNGA. The galaxy as observed with CALIFA is analysed with the spectral fitting code STARLIGHT, and is compared to the results from P-MaNGA observations with both FIREFLY analysis and analysis with PPXF as described in Section 5.6.

6 COMPARISONS WITH OTHER P-MANGA ANALYSES

In this section, we compare the analyses in this paper with other current analyses of the P-MaNGA data.

6.1 Emission line ratios

Emission line ratios are a powerful tool to study the state of the ionized gas in galaxies. The Baldwin–Phillips–Terlevich (BPT; Baldwin, Phillips & Terlevich 1981; Veilleux & Osterbrock 1987) diagram, making use of the line ratios [N II] λ6584/Hα and [O III]λ5007/Hβ, is the most popular diagnostic used to distinguish ionization due to star formation from ionization due to other sources, including active galactic nuclei (AGN), low-ionization nuclear emission-line regions (LINERs) and shocks. A detailed analysis of the ionized gas content of the P-MaNGA galaxies using the BPT diagram, complemented with other diagnostics, is presented in Belfiore et al. (2014).

In this section, we compare the results of the BPT classification with stellar ages and metallicities derived in this paper from full spectral fitting. We make use of the emission lines maps created by Belfiore et al. (2014) and plot in Fig. 17 the position of all the regions in the 14 galaxies considered by Belfiore et al. (2014) in the BPT diagram. Belfiore et al. (2014) discuss a comparison with D4000 and Hδ absorption. Here, we extend this analysis by directly comparing with stellar population ages and metallicities. We make use of the demarcation lines of Kewley et al. (2001) and Kauffmann et al. (2003b). We refer the reader to Belfiore et al. (2014) for a careful discussion of the assumptions and caveats implicit in the use of these demarcation lines. We expect galactic regions (Voronoi bins) which lie below the demarcation Kauffmann et al. (2003b) line to harbour ongoing star formation in H II regions. This is confirmed by the study of the stellar population ages, as evident in the left-hand side of Fig. 17, where the regions lying below the Kauffmann

Downloaded from https://academic.oup.com/mnras/article-abstract/449/1/328/1317763
by Haverford College user
on 15 February 2018

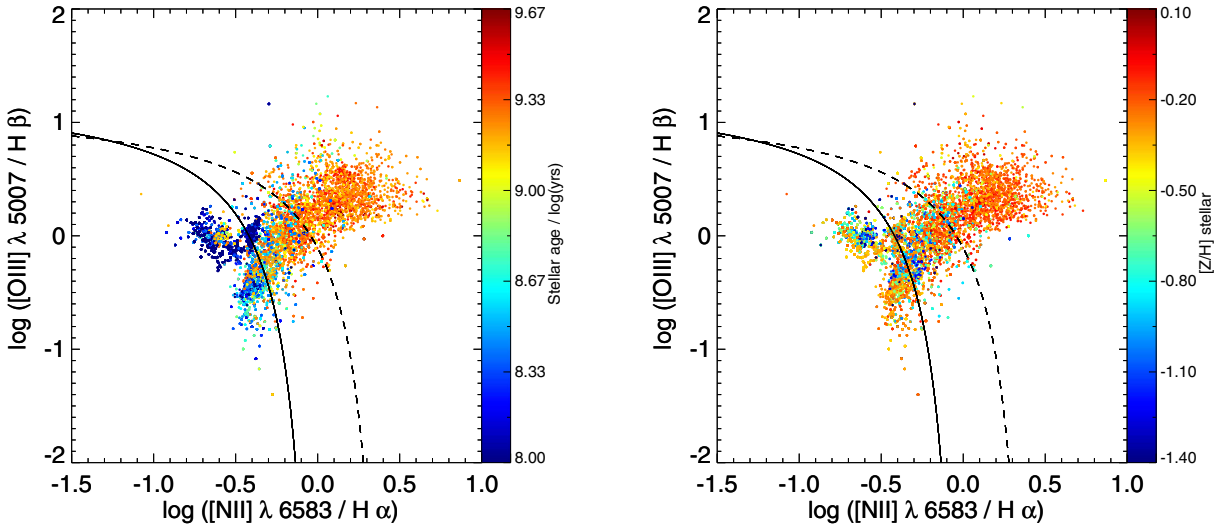

Figure 17. Emission line ratios as derived in Belfiore et al. (2014) as a function of light-weighted stellar ages (left) and metallicities (right) as derived in this paper. Overplotted are demarcation lines from Kewley et al. (2001) and Kauffmann et al. (2003b). Each pixel from all of their sub-sample of P-MaNGA galaxies is plotted following the binning scheme used in Belfiore et al. (2014).

et al. (2003b) line present younger stellar populations, consistently with a significant population of O and B stars, capable of ionizing classical H II regions.

We wish to remark on the cluster of young points ($t \sim 100$ Myr) which lie just across the Kauffmann et al. (2003b) line: these all belong to a single galaxy (p11-19C) which is experiencing a starburst. This galaxy is found by Belfiore et al. (2014) to be nitrogen enriched and hence appearing to cross over into the 'Composite' region of the BPT diagram, between the two demarcation lines, although its ionization is fully compatible with star formation.

It is very interesting to note that, as we move away from the star-forming sequence in the BPT diagram towards the 'right-wing', inhabited by AGN and LINERs, we see progressively older stellar populations. There is a tantalizing hint that the regions lying at higher [N II]/Hα, generally associated with LINERs, are older than the regions at lower [N II]/Hα, generally associated with AGN. Larger statistics and a bona fide AGN sample is needed to make further progress in the study of stellar populations of AGN and LINER hosts, but the results from these preliminary observations seem to confirm trends already observed in SDSS for the global galaxy population (Kauffmann et al. 2003b; Kewley et al. 2006; Cid Fernandes et al. 2010). This analysis also confirms the more simplistic conclusions reached using stellar populations indices ($D_N(4000)$ and EW(Hδ_A)) in Belfiore et al. (2014) and Li et al. (2015).

The right-hand side of Fig. 17 shows BPT diagram colour-coded by stellar metallicity. We see that AGN hosts have more metal-rich stellar populations, most likely because they are more massive, which would then give a mass–metallicity relationship as described in e.g. Thomas et al. (2010). In the star-forming regions, on the other hand, we see a variety of stellar metallicities from relatively metal poor to metal rich. The pixels with metal-poor populations are mostly found at high [O III]/Hβ ratio, coinciding with regions of low metallicity in the gas (Shields & Searle 1978).

6.2 Absorption and emission line diagnostics

Li et al. (2015) perform emission- and absorption-line fitting to obtain 2D maps and radial gradients of the D_{4000} Angstrom break and the equivalent widths of Hδ_A absorption and Hα emission for the P-MaNGA data set. They categorize the data set into two groups; 'centrally quiescent/passive', where the D_{4000} break in the central pixel of the P-MaNGA data cube of the galaxy observed is above 1.6, and 'centrally star forming', where the D_{4000} break is below 1.6. They find that their centrally star-forming galaxies generally have very weak radial variation in these diagnostics, whereas the gradients of centrally quiescent galaxies are significant.

We compare their results to the ages and metallicities obtained from spectral fitting in two sets of figures, first to assess how well their indices trace our results, and secondly to see whether we recover similar gradients as a function of galaxy group. We note that plate 11 galaxies, identified in this paper as being the most difficult to recover smooth gradients from, are excluded from their analysis due to being unable to obtain reliable diagnostic measurements. Fig. 18 shows the pixel-by-pixel Hδ_A and D_{4000} as a function of this paper's recovered ages and metallicities.

As expected, we see a clear dependence of both D_{4000} and EW($H\alpha$) with both age (Kauffmann et al. 2003b; Kauffmann 2014) and metallicity (Davidge & Grinder 1995; Worthey & Ottaviani 1997; Maraston 2005), as well as some scatter which could be due to other dependences such as dust attenuation and element abundance ratios (Thomas, Maraston & Korn 2004; Sánchez et al. 2012) as well as observational errors and statistical errors in the spectral fitting. We confirm a clear dependence on age, which becomes flatter as metallicity decreases, for both indices (see Maraston 2005). We see that there is an approximately 0.1 in D_{4000} and 1.0 in EW($H\delta_A$) scatter.

We note that there are two branches of high metallicity, high age points in the Hδ_A plot that are not visible in the D_{4000} plot. The bifurcation is due to most of the high metallicity points coming from a single galaxy in the sample, galaxy p9-127B, which is the dust lane clumpy galaxy shown in Fig. 2. The galaxy has high metallicity (above $\langle[Z/H]\rangle_L > 0.05$), high age ($\langle\log \text{age}\rangle_L > 5$ Gyr) and high D_{4000} (>1.8) across all of the bulge and most of the disc, except the dust lane region where these values are much lower. However, the EW(Hδ_A) has a large asymmetry between the two sides of the core along the major axis that transitions quickly between very low (~ -2) to more moderate (~ 0) values, giving rise to the appearance

Downloaded from https://academic.oup.com/mnras/article-abstract/449/1/328/1317763
by Haverford College user
on 15 February 2018

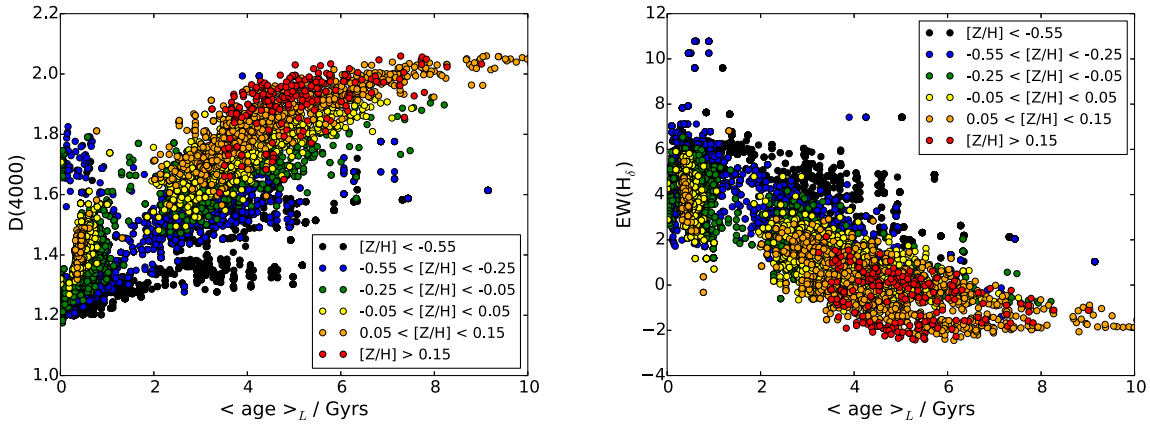

Figure 18. D_{4000} and EW($H\alpha$) measurements from Li et al. (2015) as a function of the light-weighted stellar ages and metallicities (colour-coded) derived in this paper. Each pixel from all of their sub-sample of P-MaNGA galaxies is plotted following the binning scheme used in Belfiore et al. (2014).

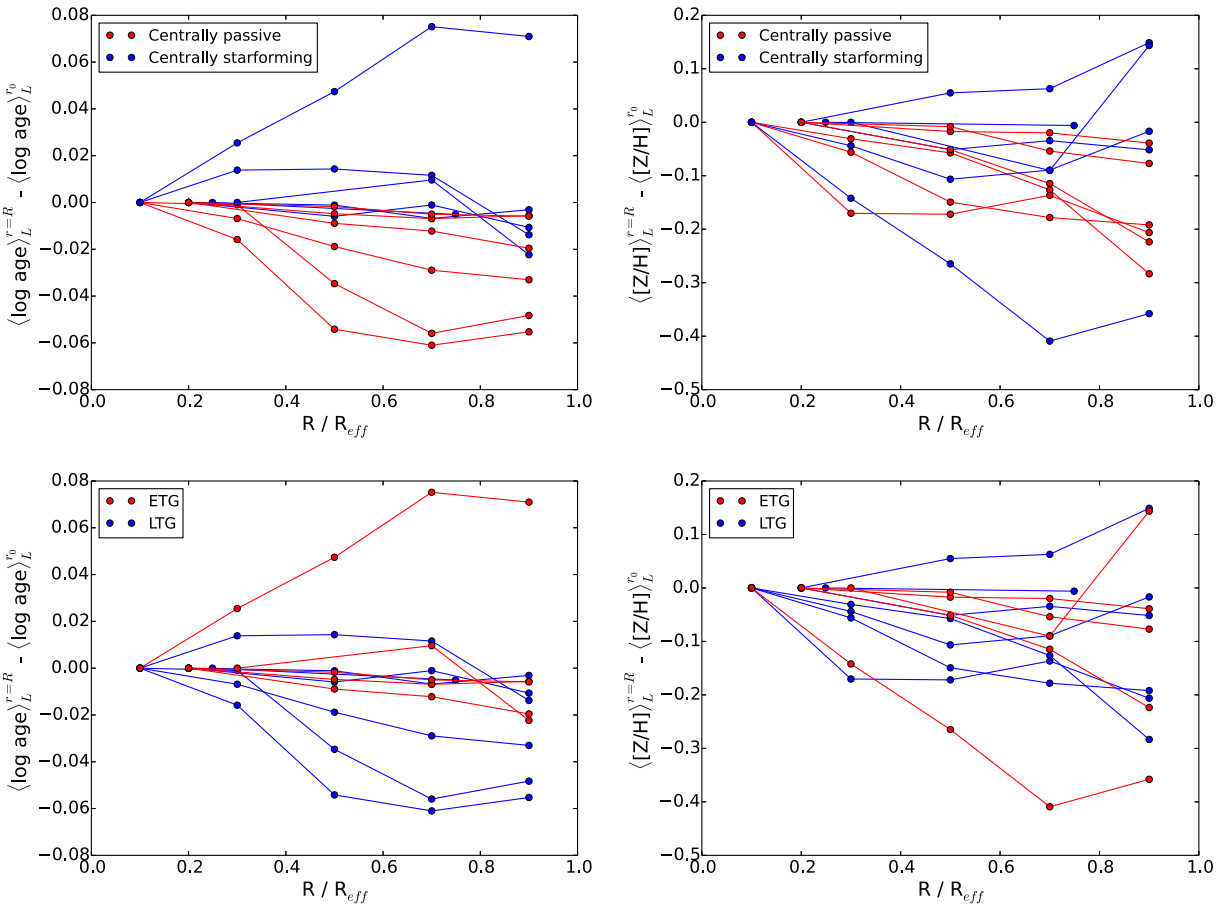

Figure 19. Light-weighted age and metallicity gradients up to 1 effective radius, plotted as the change in age/metallicity from the first elliptical annular bin, where each line represents the profile from a P-MaNGA galaxy. In the upper panels, we use the classifications of centrally quiescent/passive or centrally star forming as described in Li et al (2015). In the lower panels, we use the morphological classifications in this paper (as in Table 2). Bins are 0.2 effective radius in size to match Li et al. (2015) as much as possible; however, we impose a condition that each bin must contain at least 10 pixels from the corresponding data cube. If this condition is not met, we sample at wider bins until the criterion is met, in order to ensure a reliable mean age or metallicity at each point.

of two fairly distinct branches in the Hδ_A plot. The physical explanation for why this asymmetry exists in this galaxy in Hδ_A and not the other properties is not currently known.

In Fig. 19, we use the same plotting and binning conventions used in Li et al. (2015), binning our properties in 0.2 effective radius annular bins and measuring the difference in age and metallicity determined from the first bin (r_0). We use classifications based on measured D_{4000} in the central pixel of each galaxy in the upper panels, and use the same morphological classification as used in Table 2 in the lower panels.

Downloaded from https://academic.oup.com/mnras/article-abstract/449/1/328/1317763
by Haverford College user
on 15 February 2018

Encouragingly, we see that age gradients are clearly the main driver of the split between centrally quiescent and centrally star-forming galaxies, with metallicity gradients showing no clear divide between the two. We emphasize that this result is not in conflict with the gradient results presented earlier. The centrally quenched galaxies in Li et al. (2015) contain a mix of different morphologies, and in particular include objects in which the combination of a passive central bulge with a star-forming disc result in the age gradients measured. If we separate again by morphology as in Section 5.1, we recover the conclusions presented in that section as shown by Fig. 10. We note that compared to the gradients derived in Fig. 10, we only analyse up to 1 R_e in this figure to match Li et al. (2015), hence we do not probe the outer regions of the early-type galaxies which will typically have a lower metallicity stellar component and therefore a more negative gradient.

We find that age gradients in late-type galaxies are typically negative whereas the early-type galaxies are typically flat. The metallicity gradients of late-type galaxies show no clear separation, while the early-type galaxies have on average more negative gradients. This shows that the clear distinction in age and metallicity gradients between centrally quiescent and centrally star-forming galaxies as discussed in Li et al. (2015) is mostly driven by bulge–disc transition. Such a transition will be more clearly identifiable in the full MaNGA sample.

7 CONCLUSIONS

We have shown and discussed the first application of full spectral fitting of stellar population models to P-MaNGA galaxy data, a prototypical data release preceding the start of the actual MaNGA IFU galaxy survey (Bundy et al. 2015). We embarked in this work for several reasons, namely exploring the capabilities of our fitting and modelling method to unveil the physical parameters of galaxies and study our success as a function of observational conditions, exposure times, and galaxy type. As a hotspot of our approach, we introduce a method to deal with dust attenuation that by removing the large-scale features of spectra such as the continuum before fitting, allow us to fit unattenuated spectra and to then derive very accurate dust values. We calibrate the method by using galaxies which display dust lanes in their optical images as well as mock galaxies with known dust input. We show that we can accurately recover the dust displacement in the stellar population maps. This now allows us to calculate other stellar population properties that are more accurate and physically plausible, such as radially symmetric stellar mass maps.

We present our calculations as 2D maps of age, metallicity, dust, and stellar mass and their corresponding radial profiles and gradients. Since the P-MaNGA data contain a varied selection of galaxy types, we show that we are able to recover many different features and structures in this data, such as spiral arms, additional galaxy components, clear radial profiles for spheroidal galaxies, and artefacts in the data. This will be a superlative tracer of galaxy evolution.

We derive radial profiles of age, metallicity, and stellar mass for all of the P-MaNGA data. We show that the mass profiles are in general very smooth as a function of radius. Age and metallicity profiles can show unevenness, which depends on the quality of observations. We notice that the maps of poorly observed or noisy galaxies display an increased variance on the Voronoi bins which create fake structures, but most importantly erase the signature of real structures as spiral arms.

Importantly for galaxy evolution studies, we derive the radial gradients of stellar population properties. We find that metallicity gradients are negative for spheroids (-0.15 dex/R_e), compared to the flat gradients of late-type galaxies, which is consistent with previous knowledge. Age gradients are also negative for late type galaxies (-0.39 dex/R_e), though almost negligible for spheroids, which is again consistent with the literature. We calculate statistical errors on the radial profiles and gradients obtained as a function of observational quality, comprised of S/N, airmass, and exposure times, which we will use to calibrate analysis of MaNGA data.

Additionally, we demonstrate that the stellar mass density profiles remain relatively unchanged as a function of three stellar population model input stellar spectral libraries, even if we find $\sim$0.1 dex differences in the age and metallicity profiles. None the less, the overall set of gradients for the P-MaNGA data sample is consistent across the three model libraries. Additionally, we show that the recovery of spatial features in age and metallicity is consistent across model, fitting code, fitting parameters, and the CALIFA survey.

Lastly, we show how comparisons with analyses of the absorption and emission features MaNGA data can shed light on galaxy evolution questions such as inside–out growth and/or quenching, and studies of AGN.

This work will proceed with the analysis of the full MaNGA data set in the future, and constitutes the basis of our understanding of the performances of full spectral fitting on MaNGA-type IFU data.

ACKNOWLEDGEMENTS

Funding for SDSS-III and SDSS-IV has been provided by the Alfred P. Sloan Foundation and Participating Institutions. Additional funding for SDSS-III comes from the National Science Foundation and the US Department of Energy Office of Science. Further information about both projects is available at www.sdss3.org.

SDSS is managed by the Astrophysical Research Consortium for the Participating Institutions in both collaborations. In SDSS-III, these include the University of Arizona, the Brazilian Participation Group, Brookhaven National Laboratory, Carnegie Mellon University, University of Florida, the French Participation Group, the German Participation Group, Harvard University, the Instituto de Astrofisica de Canarias, the Michigan State/Notre Dame/JINA Participation Group, Johns Hopkins University, Lawrence Berkeley National Laboratory, Max Planck Institute for Astrophysics, Max Planck Institute for Extraterrestrial Physics, New Mexico State University, New York University, Ohio State University, Pennsylvania State University, University of Portsmouth, Princeton University, the Spanish Participation Group, University of Tokyo, University of Utah, Vanderbilt University, University of Virginia, University of Washington, and Yale University.

The Participating Institutions in SDSS-IV are Carnegie Mellon University, Colorado University, Boulder, Harvard–Smithsonian Center for Astrophysics Participation Group, Johns Hopkins University, Kavli Institute for the Physics and Mathematics of the Universe Max-Planck-Institut fuer Astrophysik (MPA Garching), Max-Planck-Institut fuer Extraterrestrische Physik (MPE), Max-Planck-Institut fuer Astronomie (MPIA Heidelberg), National Astronomical Observatory of China, New Mexico State University, New York University, The Ohio State University, Penn State University, Shanghai Astronomical Observatory, United Kingdom Participation Group, University of Portsmouth, University of Utah, University of Wisconsin, and Yale University.

The authors would like to thank Sebastian F. Sanchez for his very useful and detailed comments and to Roberto Cid Fernandes for providing access to the CALIFA data used in Fig. 16.

Downloaded from https://academic.oup.com/mnras/article-abstract/449/1/328/1317763
by Haverford College user
on 15 February 2018

Numerical computations were done on the Sciama High Performance Compute (HPC) cluster which is supported by the ICG, SEPNet, and the University of Portsmouth.

MC acknowledges support from a Royal Society University Research Fellowship.

REFERENCES

Adelman-McCarthy J. K. et al., 2008, ApJS, 175, 297
Aihara H. et al., 2011, ApJS, 193, 29
Annibali F., Bressan A., Rampazzo R., Zeilinger W. W., Danese L., 2007, A&A, 463, 455
Bacon R. et al., 2001, MNRAS, 326, 23
Baldwin J. A., Phillips M. M., Terlevich R., 1981, PASP, 93, 5
Barker M. K., Sarajedini A., Geisler D., Harding P., Schommer R., 2007, AJ, 133, 1138
Beifiori A., Maraston C., Thomas D., Johansson J., 2011, A&A, 531, A109
Belfiore F. et al., 2014, MNRAS, preprint (arXiv:1410.7781)
Bershady M. A., Verheijen M. A. W., Swaters R. A., Andersen D. R., Westfall K. B., Martinsson T., 2010, ApJ, 716, 198
Blanc G. A. et al., 2013, AJ, 145, 138
Bruzual G., Charlot S., 2003, MNRAS, 344, 1000
Bundy K. et al., 2015, ApJ, 798, 7
Calzetti D., Armus L., Bohlin R. C., Kinney A. L., Koornneef J., Storchi-Bergmann T., 2000, ApJ, 533, 682
Cappellari M., Copin Y., 2003, MNRAS, 342, 345
Cappellari M., Emsellem E., 2004, PASP, 116, 138
Cappellari M. et al., 2011, MNRAS, 413, 813
Chen Y.-M. et al., 2012, MNRAS, 421, 314
Cid Fernandes R., Mateus A., Sodré L., Stasińska G., Gomes J. M., 2005, MNRAS, 358, 363
Cid Fernandes R., Stasińska G., Schlickmann M. S., Mateus A., Vale Asari N., Schoenell W., Sodré L., 2010, MNRAS, 403, 1036
Cid Fernandes R. et al., 2013, A&A, 557, A86
Conroy C., van Dokkum P. G., 2012, ApJ, 760, 71
Conroy C., Gunn J. E., White M., 2009, ApJ, 699, 486
Croom S. M. et al., 2012, MNRAS, 421, 872
Davidge T. J., Grinder M., 1995, AJ, 109, 1433
Dawson K. S. et al., 2013, AJ, 145, 10
Driver S. P. et al., 2011, MNRAS, 413, 971
Drory N. et al., 2015, AJ, 149, 77
Eisenstein D. J. et al., 2011, AJ, 142, 72
Falcón-Barroso J., Sánchez-Blázquez P., Vazdekis A., Ricciardelli E., Cardiel N., Cenarro A. J., Gorgas J., Peletier R. F., 2011, A&A, 532, A95
Ferreras I., La Barbera F., de la Rosa I. G., Vazdekis A., de Carvalho R. R., Falcón-Barroso J., Ricciardelli E., 2013, MNRAS, 429, L15
Fioc M., Rocca-Volmerange B., 1997, A&A, 326, 950
Folkes S. et al., 1999, MNRAS, 308, 459
Fukugita M., Ichikawa T., Gunn J. E., Doi M., Shimasaku K., Schneider D. P., 1996, AJ, 111, 1748
Gerssen J., Wilman D. J., Christensen L., 2012, MNRAS, 420, 197
González Delgado R. M., Cerviño M., Martins L. P., Leitherer C., Hauschildt P. H., 2005, MNRAS, 357, 945
González Delgado R. M. et al., 2014, A&A, 562, A47
Gunn J. E. et al., 2006, AJ, 131, 2332
Gustafsson B., Edvardsson B., Eriksson K., Jørgensen U. G., Nordlund Å., Plez B., 2008, A&A, 486, 951
Iglesias-Páramo J. et al., 2013, A&A, 553, L7
Johansson J., Thomas D., Maraston C., 2012, MNRAS, 421, 1908
Kauffmann G., 2014, MNRAS, 441, 2717
Kauffmann G. et al., 2003a, MNRAS, 341, 33
Kauffmann G. et al., 2003b, MNRAS, 346, 1055
Kewley L. J., Dopita M. A., Sutherland R. S., Heisler C. A., Trevena J., 2001, AJ, 556, 121
Kewley L. J., Groves B., Kauffmann G., Heckman T., 2006, MNRAS, 372, 961
Kobayashi C., Arimoto N., 1999, ApJ, 527, 573
Kroupa P., 2001, MNRAS, 322, 231
Kuntschner H. et al., 2010, MNRAS, 408, 97
Kurucz R. L., 1979, ApJS, 40, 1
Lançon A., Wood P. R., 2000, A&AS, 146, 217
Le Borgne J.-F. et al., 2003, A&A, 402, 433
Leitherer C. et al., 1999, ApJS, 123, 3
Li C. et al., 2015, ApJ, preprint (arXiv:1502.07040)
Liddle A. R., 2007, MNRAS, 377, L74
MacArthur L. A., González J. J., Courteau S., 2009, MNRAS, 395, 28
Maraston C., 1998, MNRAS, 300, 872
Maraston C., 2005, MNRAS, 362, 799
Maraston C., Strömbäck G., 2011, MNRAS, 418, 2785 (M11)
Maraston C., Daddi E., Renzini A., Cimatti A., Dickinson M., Papovich C., Pasquali A., Pirzkal N., 2006, ApJ, 652, 85
Maraston C. et al., 2013, MNRAS, 435, 2764
Mehlert D., Thomas D., Saglia R. P., Bender R., Wegner G., 2003, A&A, 407, 423
Ocvirk P., Pichon C., Lançon A., Thiébaut E., 2006, MNRAS, 365, 46
Pforr J., Maraston C., Tonini C., 2012, MNRAS, 422, 3285
Prugniel P., Soubiran C., Koleva M., Le Borgne D., 2007, preprint (astro-ph/0703658)
Prugniel P., Vauglin I., Koleva M., 2011, A&A, 531, A165
Rawle T. D., Smith R. J., Lucey J. R., Swinbank A. M., 2008, MNRAS, 389, 1891
Saglia R. P., Maraston C., Greggio L., Bender R., Ziegler B., 2000, A&A, 360, 911
Saglia R. P., Maraston C., Thomas D., Bender R., Colless M., 2002, ApJ, 579, L13
Salpeter E. E., 1955, ApJ, 121, 161
Sánchez S. F. et al., 2012, A&A, 538, A8
Sánchez-Blázquez P. et al., 2006, MNRAS, 371, 703
Sánchez-Blázquez P., Forbes D. A., Strader J., Brodie J., Proctor R., 2007, MNRAS, 377, 759
Sánchez-Blázquez P., Ocvirk P., Gibson B. K., Pérez I., Peletier R. F., 2011, MNRAS, 415, 709
Sánchez-Blázquez P. et al., 2014, A&A, 570, A6
Sarzi M. et al., 2006, MNRAS, 366, 1151
Sharp R. et al., 2015, MNRAS, 446, 1551
Shields G. A., Searle L., 1978, ApJ, 222, 821
Smee S. A. et al., 2013, AJ, 146, 32
Spiniello C., Trager S., Koopmans L. V. E., Conroy C., 2014, MNRAS, 438, 1483
Tamura N., Kobayashi C., Arimoto N., Kodama T., Ohta K., 2000, AJ, 119, 2134
Thomas D., Maraston C., Bender R., 2003, MNRAS, 339, 897
Thomas D., Maraston C., Korn A., 2004, MNRAS, 351, L19
Thomas D., Maraston C., Bender R., Mendes de Oliveira C., 2005, ApJ, 621, 673
Thomas D., Maraston C., Schawinski K., Sarzi M., Silk J., 2010, MNRAS, 404, 1775
Thomas D., Maraston C., Johansson J., 2011, MNRAS, 412, 2183
Thomas D. et al., 2013, MNRAS, 431, 1383
Tojeiro R., Heavens A. F., Jimenez R., Panter B., 2007, MNRAS, 381, 1252
Vazdekis A., Casuso E., Peletier R. F., Beckman J. E., 1996, ApJS, 106, 307
Vazdekis A., Sánchez-Blázquez P., Falcón-Barroso J., Cenarro A. J., Beasley M. A., Cardiel N., Gorgas J., Peletier R. F., 2010, MNRAS, 404, 1639
Veilleux S., Osterbrock D. E., 1987, ApJS, 63, 295
Williams B. F., Dalcanton J. J., Dolphin A. E., Holtzman J., Sarajedini A., 2009, ApJ, 695, L15
Worthey G., Ottaviani D. L., 1997, ApJS, 111, 377
Wu H., Shao Z., Mo H. J., Xia X., Deng Z., 2005, ApJ, 622, 244
Wuyts S. et al., 2012, ApJ, 753, 114
Yoachim P., Dalcanton J. J., 2008, ApJ, 683, 707
York D. G. et al., 2000, AJ, 120, 1579

Downloaded from https://academic.oup.com/mnras/article-abstract/449/1/328/1317763
by Haverford College user
on 15 February 2018

APPENDIX A

In this appendix, we provide the stellar population maps and radial profiles of the P-MaNGA galaxies described briefly in the results section, but not shown there to avoid disrupting the flow of the paper with detail about individual galaxies. As in the results section, we split our analyses by groups as described in Table 2.

A1 Additional maps: Group α

Galaxy p9-19D (Fig. A1) has been observed with MaNGA-like data quality with 3 h exposures, decent (1.7 arcsec) seeing conditions, and is in the MaNGA primary sample selection. It is an early-type galaxy that has been observed with the N_{19} IFU setup. We see a high level of radial symmetry in the age, metallicity, and stellar mass density maps. It has a $\langle \log \mathrm{age} \rangle_L = 6$ Gyr/$\langle \log \mathrm{age} \rangle_M = 8$ Gyr, somewhat supersolar metallicity core going down to $\langle \log \mathrm{age} \rangle_L = \langle \log \mathrm{age} \rangle_M = 5$ Gyr with approximately solar metallicity at above 1 effective radius, and shows little signs of dust. It therefore has quite clear, albeit weak, negative age, and metallicity gradients.

Galaxies p9-19E (Fig. A2) and p9-127B (Fig. A3) have N_{19} and N_{127} IFU observations covering 2.2 and 2.4 effective radii, respectively. The early-type galaxy p9-19E shows a much flatter age and metallicity profile and is considerably younger in $\langle \log \mathrm{age} \rangle_L$ than the primary-selected early-type galaxies, though similar $\langle \log \mathrm{age} \rangle_M$ to other galaxies in the sample, with evidence of a possibly younger core in the population maps that is washed out with the intermixed older population in the radial profile. This suggest recent star formation is well mixed within most of the galaxy, giving the maps a clumpy structure.

Conversely, galaxy p9-127B (Fig. A3) is an edge-on late-type galaxy with a very clumpy structure, as evidenced clearly in the dust attenuation map. The galaxy as a whole is relatively young ($\langle \log \mathrm{age} \rangle_L = 0.8$ Gyr/$\langle \log \mathrm{age} \rangle_M = 2$ Gyr on average), but also has some regions of older populations, on average 1 Gyr older and more metal poor (-0.50 dex or less) in a ring around the central kpc core. This is visible in the radial profiles in both age and metallicity as a peak and a dip, respectively, in these properties at low radius. In age, this trend turns over to give a negative gradient but in metallicity it rises again at 1.0 R_e to give a positive gradient on average.

A2 Additional maps: Group β

Galaxy p9-127A (Fig. A4) is identified very clearly in the light-weighted population maps as a galaxy with an old (8 Gyr) metal-rich ($[Z/H] = 0.2$) core with a younger (1–2 Gyr) and less metal-rich ($[Z/H] = -0.2$) outer population, which matches in position with the imaging data as corresponding to the inner part of the spiral arm structure. The mass-weighted properties shows a flatter structure across the galaxy, suggesting that the star formation in the spiral arms are the main driver of the structure in the light-weighted properties. As mentioned earlier, the large difference between mass-weighted and light-weighted age indicates a more continuous star formation history, consistent with spiral arm star formation histories. This spiral structure is also traced in the dust attenuation maps. We note the presence of a foreground star on top of the image, which we mask over in the radial profiles by applying a recessional velocity cut in the data before fitting.

A3 Additional maps: Group γ

Galaxy p4-19B (Fig. A5) is a late-type galaxy with a fairly complex structure in its stellar population maps. We see a band of $\langle \log \mathrm{age} \rangle_M = \langle \log \mathrm{age} \rangle_L = 1$ Gyr stretching across the maps from north-east to south-west. This band is visible in the other maps as having low $\langle [Z/H] \rangle_L$ and $\langle [Z/H] \rangle_M$, but high $\langle \log \mathrm{age} \rangle_M$ compared to the background halo. This combination is suggestive an intermediate age disc population with a background old halo and/or disc population, with a high contribution of star formation in the outer disc regions of the galaxy giving a significant negative age gradient in $\langle \log \mathrm{age} \rangle_L$ or a flat gradient in $\langle \log \mathrm{age} \rangle_M$.

Downloaded from https://academic.oup.com/mnras/article-abstract/449/1/328/1317763
by Haverford College user
on 15 February 2018

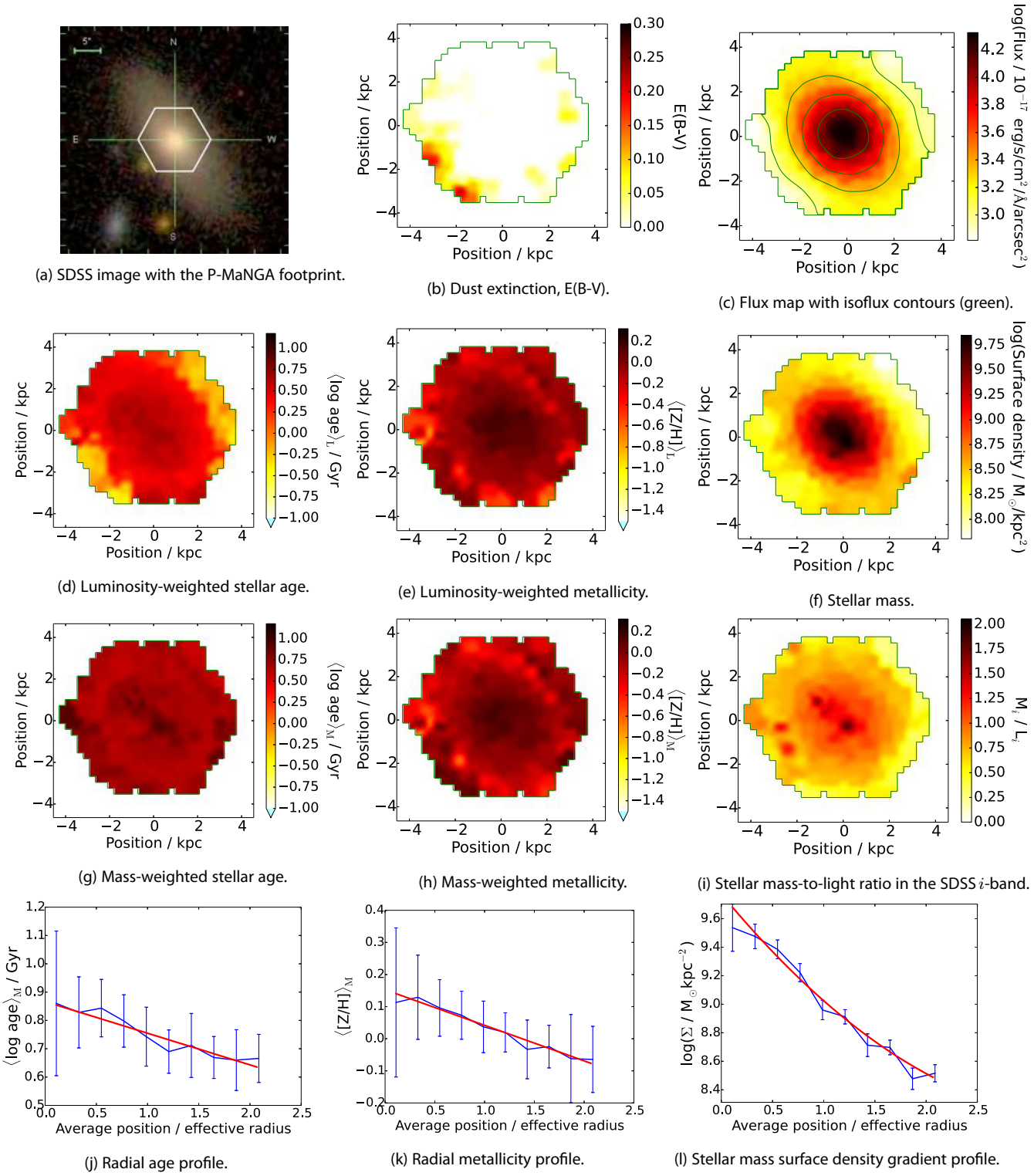

Figure A1. Group α, galaxy p9-19D as in Table 2. Stellar population maps and profiles analysed using MILES-based models with their full parameter range, as described in detail in Fig. 5. This galaxy, like p9-19B in Fig. 5, has been observed with good observational conditions with a MaNGA-like exposure time and dithering, and is selected in the MaNGA primary sample. Therefore, out of the P-MaNGA data set, these observations are the most similar to the expected output of the MaNGA primary sample.

Downloaded from https://academic.oup.com/mnras/article-abstract/449/1/328/1317763
by Haverford College user
on 15 February 2018

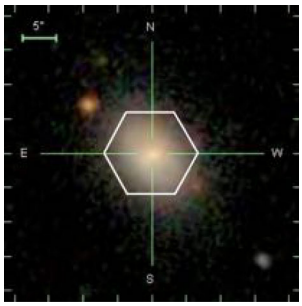

(a) SDSS image with the P-MaNGA footprint.

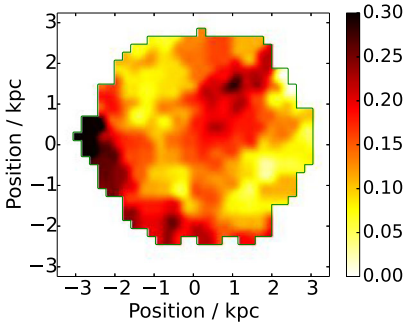

(b) Dust extinction, E(B-V).

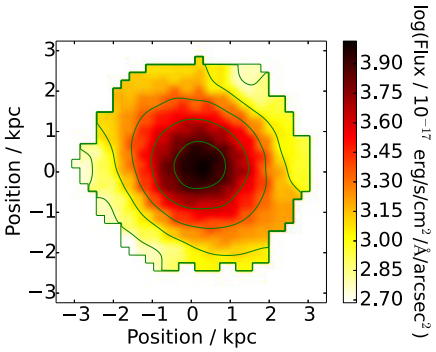

(c) Flux map with isoflux contours (green).

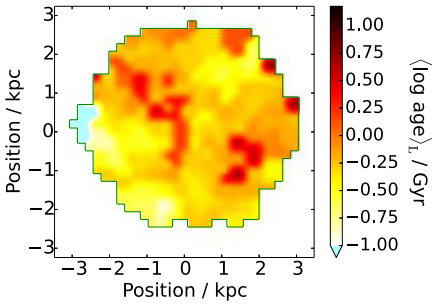

(d) Luminosity-weighted stellar age.

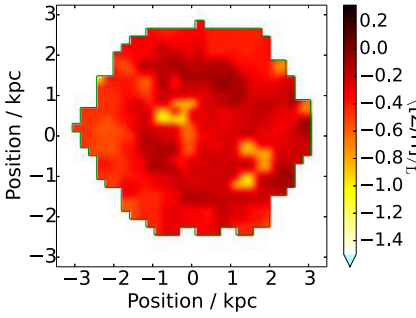

(e) Luminosity-weighted metallicity.

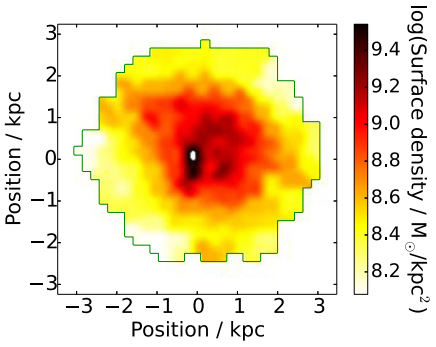

(f) Stellar mass.

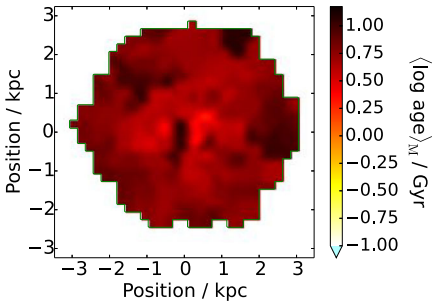

(g) Mass-weighted stellar age.

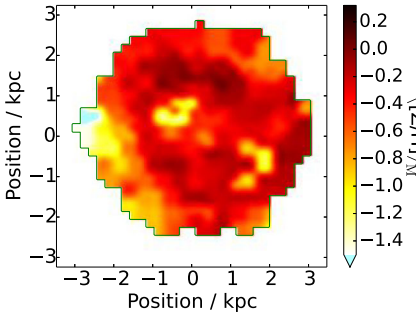

(h) Mass-weighted metallicity.

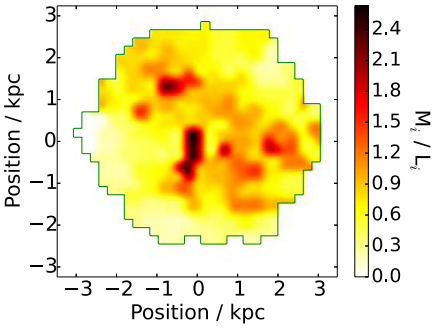

(i) Stellar mass-to-light ratio in the SDSS i-band.

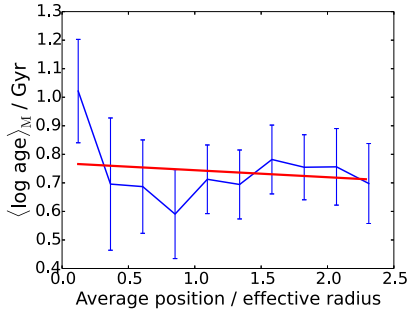

(j) Radial age profile.

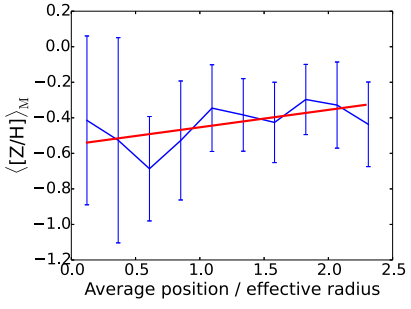

(k) Radial metallicity profile.

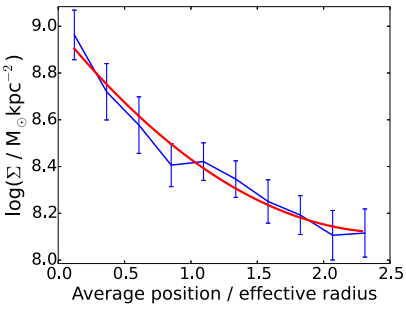

(l) Stellar mass surface density gradient profile.

Figure A2. Group α, galaxy p9-19E as in Table 2. Stellar population maps and profiles analysed using MILES-based models with their full parameter range, as described in detail in Fig. 5. This galaxy has been observed under good observational conditions with MaNGA-like exposure time and dithering, but covers a larger radial extent than would be targeted in the MaNGA primary sample. However, it is selected by the MaNGA secondary sample.

Downloaded from https://academic.oup.com/mnras/article-abstract/449/1/328/1317763
by Haverford College user
on 15 February 2018

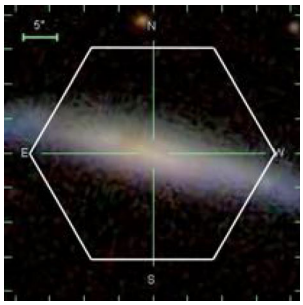

(a) SDSS image with the P-MaNGA footprint.

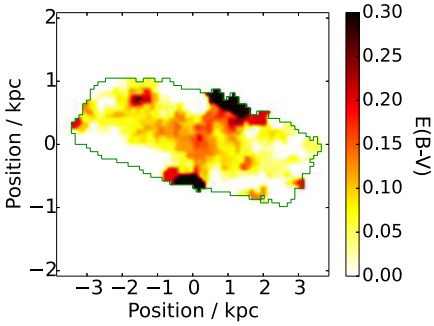

(b) Dust extinction, E(B-V).

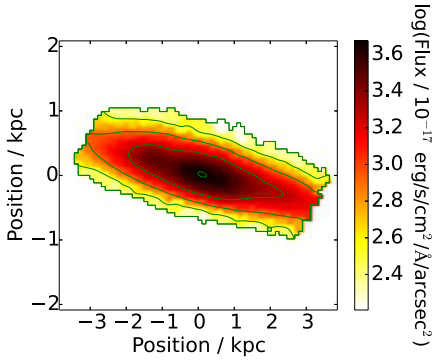

(c) Flux map with isoflux contours (green).

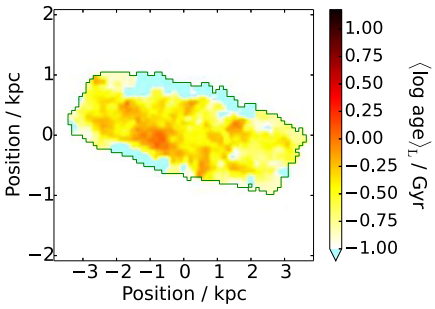

(d) Luminosity-weighted stellar age.

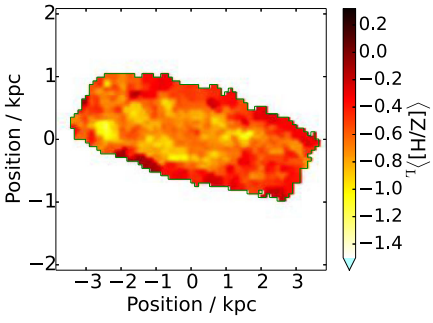

(e) Luminosity-weighted metallicity.

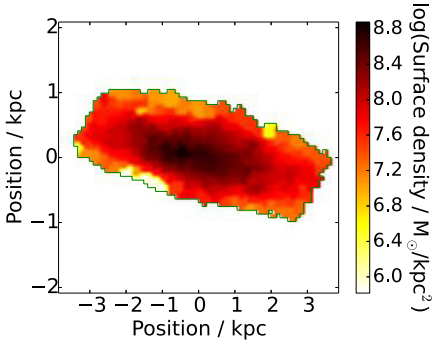

(f) Stellar mass.

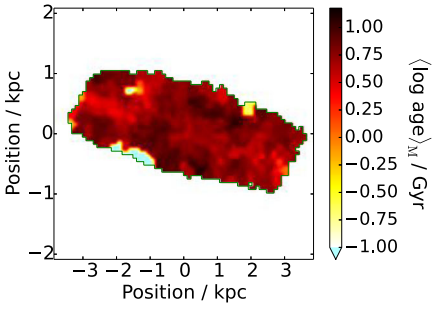

(g) Mass-weighted stellar age.

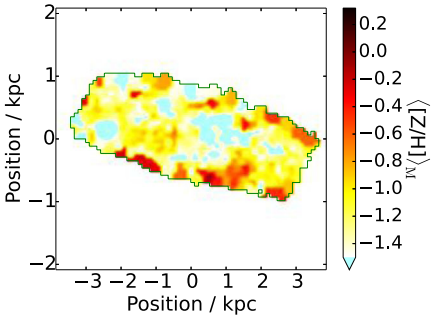

(h) Mass-weighted metallicity.

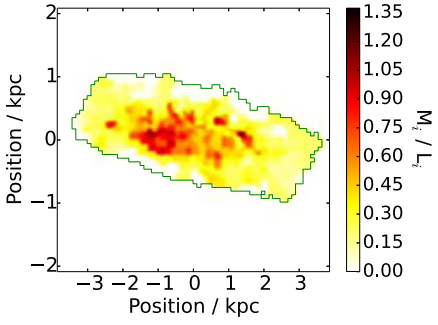

(i) Stellar mass-to-light ratio in the SDSS i-band.

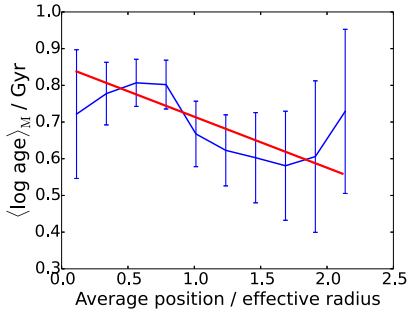

(j) Radial age profile.

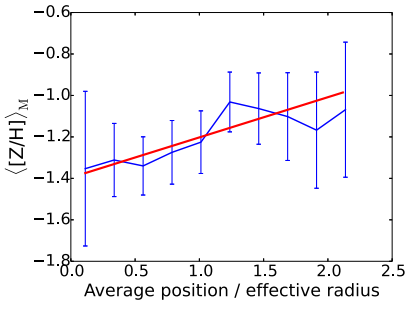

(k) Radial metallicity profile.

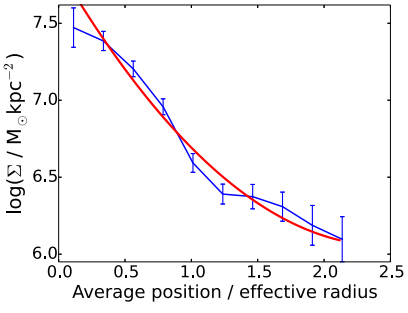

(l) Stellar mass surface density gradient profile.

Figure A3. Group α, galaxy p9-127B as in Table 2. Stellar population maps and profiles analysed using MILES-based models with their full parameter range, as described in detail in Fig. 5. This galaxy has been observed under good observational conditions with MaNGA-like exposure time and dithering, but covers a larger radial extent than would be targeted in the MaNGA primary sample, like galaxy p9-19E (Fig. A2), and is selected by the MaNGA secondary sample.

Downloaded from https://academic.oup.com/mnras/article-abstract/449/1/328/1317763
by Haverford College user
on 15 February 2018

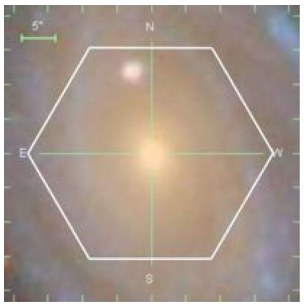

(a) SDSS image with the P-MaNGA footprint.

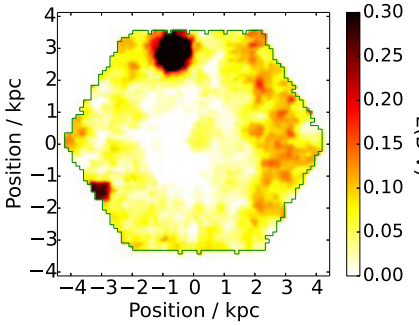

(b) Dust extinction, E(B-V).

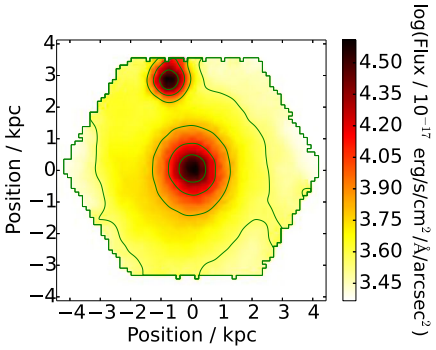

(c) Flux map with isoflux contours (green).

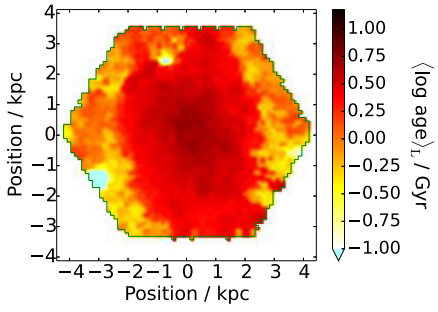

(d) Luminosity-weighted stellar age.

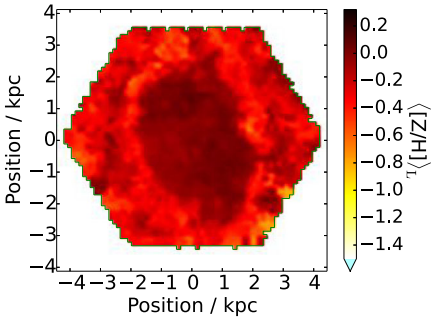

(e) Luminosity-weighted metallicity.

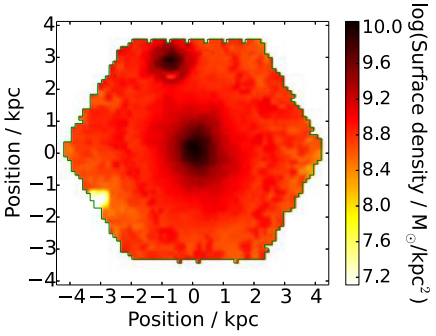

(f) Stellar mass.

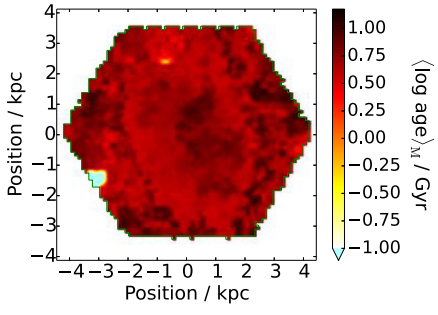

(g) Mass-weighted stellar age.

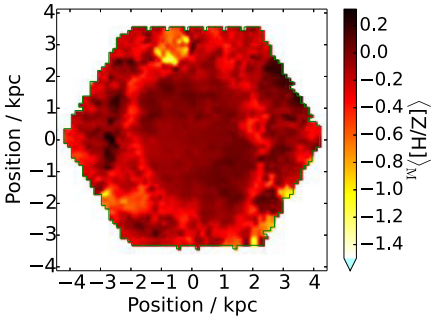

(h) Mass-weighted metallicity.

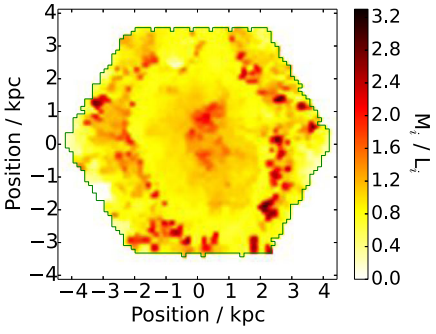

(i) Stellar mass-to-light ratio in the SDSS i-band.

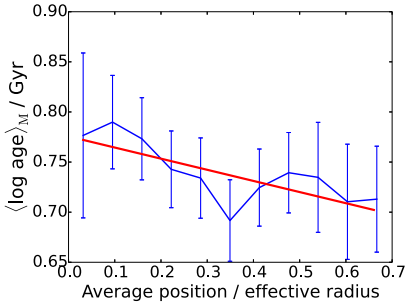

(j) Radial age profile.

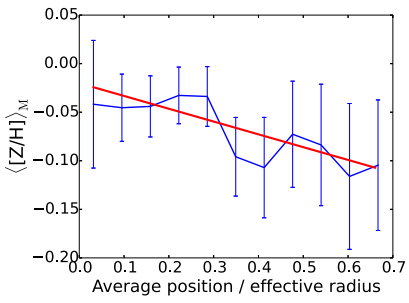

(k) Radial metallicity profile.

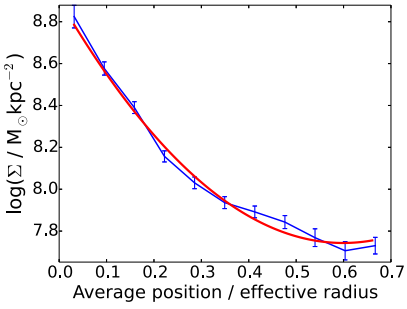

(l) Stellar mass surface density gradient profile.

Figure A4. Group β, galaxy p9-127A as in Table 2. Stellar population maps and profiles analysed using MILES-based models with their full parameter range, as described in detail in Fig. 5. This galaxy is taken under MaNGA-like observational conditions and setup, but is not targeted in the main MaNGA samples due to its low redshift, and therefore radial coverage by MaNGA IFUs. Hence, this galaxy is observed with a higher amount of structural detail then we should expect to observe with MaNGA.

Downloaded from https://academic.oup.com/mnras/article-abstract/449/1/328/1317763
by Haverford College user
on 15 February 2018

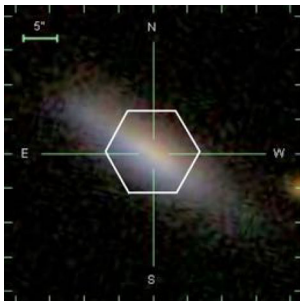

(a) SDSS image with the P-MaNGA footprint.

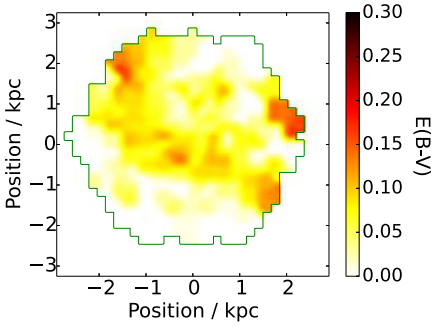

(b) Dust extinction, E(B-V).

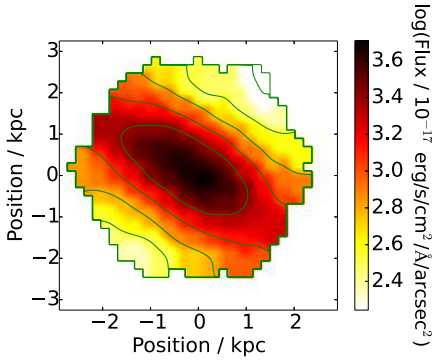

(c) Flux map with isoflux contours (green).

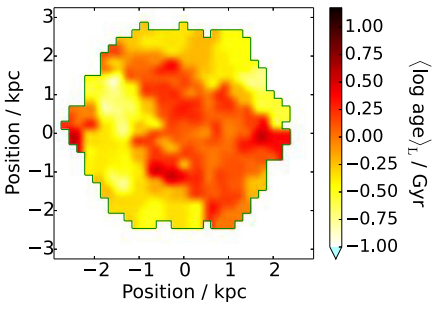

(d) Luminosity-weighted stellar age.

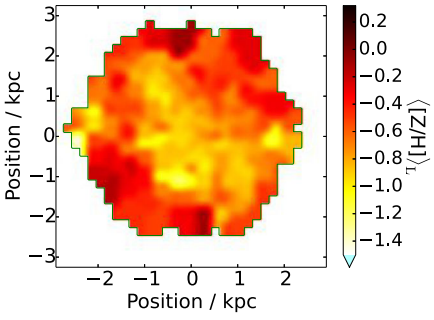

(e) Luminosity-weighted metallicity.

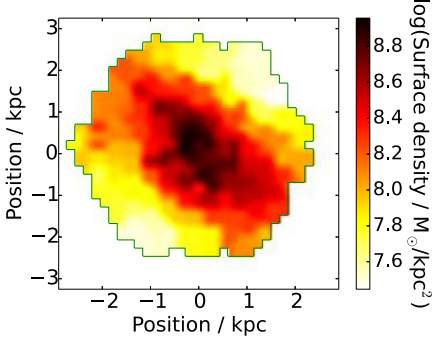

(f) Stellar mass.

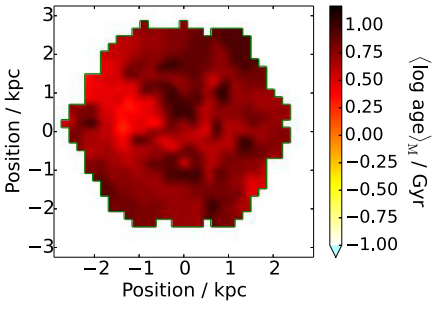

(g) Mass-weighted stellar age.

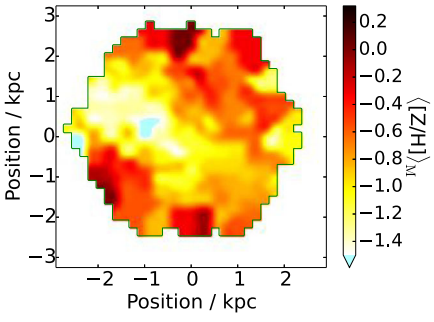

(h) Mass-weighted metallicity.

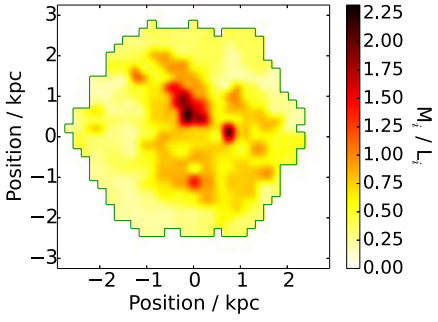

(i) Stellar mass-to-light ratio in the SDSS i-band.

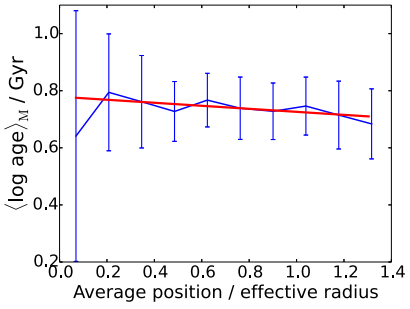

(j) Radial age profile.

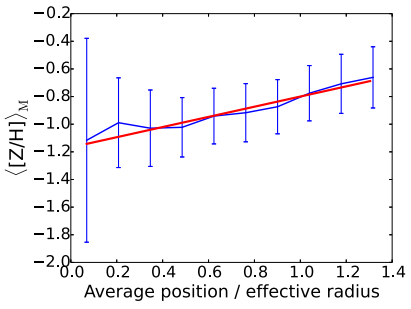

(k) Radial metallicity profile.

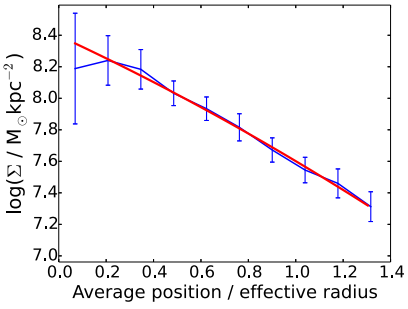

(l) Stellar mass surface density gradient profile.

Figure A5. Group γ, galaxy p4-19B as in Table 2. Stellar population maps and profiles analysed using MILES-based models with their full parameter range, as described in detail in Fig. 5. This galaxy has been observed under poorer conditions and a lower exposure and dithering setup than expected for MaNGA. Unlike galaxy p4-19C (Fig. 7), we resolve a more complex stellar population structure that reflects the asymmetric colour distribution seen in the SDSS image.

Downloaded from https://academic.oup.com/mnras/article-abstract/449/1/328/1317763
by Haverford College user
on 15 February 2018

[1]*Institute of Cosmology and Gravitation, University of Portsmouth, Portsmouth PO1 3FX, UK*
[2]*European Southern Observatory, Karl-Schwarzschild-Straße 2, D-85748 Garching bei Muenchen, Germany*
[3]*School of Physics and Astronomy, University of St Andrews, North Haugh, St Andrews KY16 9SS, UK*
[4]*Sub-department of Astrophysics, Department of Physics, University of Oxford, Denys Wilkinson Building, Keble Road, Oxford OX1 3RH, UK*
[5]*Kavli Institute for Cosmology, University of Cambridge, Madingley Road, Cambridge CB3 0HA, UK*
[6]*Cavendish Laboratory, University of Cambridge, 19 J. J. Thomson Avenue, Cambridge CB3 0HE, UK*
[7]*Department of Astronomy, University of Wisconsin-Madison, 475 N. Charter Street, Madison, WI 53706, USA*
[8]*Center for Cosmology and Particle Physics, Department of Physics, New York University, 4 Washington Place, New York, NY 10003, USA*
[9]*Kavli Institute for the Physics and Mathematics of the Universe, Todai Institutes for Advanced Study, the University of Tokyo, 277-8583 Kashiwa, Japan, (Kavli IPMU, WPI)*
[10]*Yale Center for Astronomy and Astrophysics, Yale University, New Haven, CT 06520, USA*
[11]*Dunlap Institute for Astronomy and Astrophysics, University of Toronto, 50 St George Street, Toronto, ON M5S 3H4, Canada*
[12]*McDonald Observatory, Department of Astronomy, The University of Texas at Austin, 2515 Speedway Stop C1402, Austin, TX 78712-1206, USA*
[13]*Université Lyon 1, Observatoire de Lyon, Centre de Recherche Astrophysique de Lyon and Ecole Normale Supérieure de Lyon, 9 avenue Charles André, F-69230 Saint-Genis Laval, France*
[14]*Department of Physics & Astronomy, University of Iowa, 751 Van Allen Hall, Iowa City, IA 52242, USA*
[15]*Space Telescope Science Institute, 3700 San Martin Drive, Baltimore, MD 21218, USA*
[16]*Partner Group of Max-Planck Institute for Astrophysics, Shanghai Astronomical Observatory, Nandan Road 80, Shanghai 200030, China*
[17]*Department of Physics and Astronomy, University of Kentucky, 505 Rose Street, Lexington, KY 40506-0055, USA*
[18]*Apache Point Observatory and New Mexico State University, PO Box 59, Sunspot, NM 88349-0059, USA*

This paper has been typeset from a TEX/LATEX file prepared by the author.

Downloaded from https://academic.oup.com/mnras/article-abstract/449/1/328/1317763
by Haverford College user
on 15 February 2018